Ore Geology Reviews 127 (2020) 103800

Contents lists available at ScienceDirect

Ore Geology Reviews

journal homepage: www.elsevier.com/locate/oregeorev

Native metals and intermetallic compounds in subduction-related ultramafic rocks from the Stanovoy mobile belt (Russian Far East): Implications for redox heterogeneity in subduction zones

Pavel K. Kepezhinskas [a,b,*], Nikita P. Kepezhinskas [c], Nikolai V. Berdnikov [d], Valeria O. Krutikova [d]

[a] PNK Geoscience, Tampa, FL, USA
[b] Khingan Minerals AS, Oslo, Norway
[c] Department of Earth and Atmospheric Sciences, University of Alberta, Edmonton, Alberta, Canada
[d] Kosygin Institute of Tectonics and Geophysics, Khabarovsk, Russian Federation

ARTICLE INFO

Keywords:
Subduction
Ultramafic rocks
Native metals
Intermetallic compounds
Chlorine-rich fluids

ABSTRACT

Plutonic associations in orogenic belts are potent indicators of multi-stage fractionation of primitive arc magmas and growth of island-arc crust under evolving redox conditions in ancient subduction zones. Ildeus-Lucha ultramafic–mafic complex (ILC) was emplaced at 232–233 Ma within the Mesozoic Stanovoy convergent margin and subsequently underwent multi-stage hydrothermal alteration and greenschist to amphibolite facies metamorphism (~140 Ma), followed by adakite and K-lamprophyre magmatism (114–117 Ma). Dunite, wehrlite, pyroxenite and gabbro in the ILC are composed of olivine, clinopyroxene, orthopyroxene, plagioclase and late-magmatic amphibole. Mineral compositions in the ILC are typical of island-arc plutonic complexes characterized by early crystallization of orthopyroxene, plagioclase intercumulus and presence of magmatic amphibole. Ultramafic-mafic rocks display high-field strength (HFS) element depletions coupled with large-ion lithophile (LIL) element enrichments, indicating formation via crystal fractionation of mafic primary magma derived from a subduction-related mantle source. Some ultramafic rocks from the ILC contain native metals (W, Pt, Au, Ag, Zn, Bi) and intermetallic compounds (Cu-Au-Ag, Pt-Rh-Pd, Cu-Sn-Zn, etc.) included in silicate minerals, or observed as discrete phases in the finer-grained silicate-oxide-sulfide matrix. Textural evidence and association with either primary (magmatic) or secondary (metasomatic or metamorphic) mineral phases, suggest either magmatic (high-temperature) or metasomatic (low-temperature) origin of metals and metallic compounds. The following models of their formation can be proposed on the basis of the presented data: a) crystallization (W and, possibly, Pt) from metal-rich arc magmas under unusually reduced conditions in subduction-related lithosphere; b) formation from magmatic sulfides during pervasive serpentinization and release of abiogenic hydrocarbons and c) precipitation from chlorine-rich, saline aqueous fluids associated with collision-related metasomatism of the Stanovoy island arc crust.

1. Introduction

Subduction-zone magmas and their mantle sources are enriched in chalcophile (Cu, Zn, Pb) and siderophile (Pt, Pd, Ir, Os, Ru, Rh, Au) elements reflecting high mobility of these chemical elements in hydrous slab-derived fluids and their effective transport through both slab-mantle interface as well as island-arc crust (Noll et al., 1996; McInnes et al., 1999; Kepezhinskas and Defant, 2001; Widom et al., 2003; Timm et al., 2012). The mobility of these ore metals in convergent plate settings is believed to be affected by pressure, temperature, oxygen and sulfur fugacity, as well as salinity of slab fluids, with oxygen fugacity being one of the predominant factors controlling trace element partitioning in subduction zones (Jenner et al., 2010; Pokrovsky et al., 2013; Richards, 2015; Keppler, 2017; Scambelluri et al., 2019; Grossley et al., 2020). Subduction zones, in general, are highly oxidized environments in comparison to oceanic lithosphere as suggested by the redox state of arc peridotites (Brandon and Draper, 1996; Parkinson and Arculus, 1999; Ionov, 2010), arc ultramafic cumulates (Ballhaus, 1993; Bucholz

* Corresponding author at: PNK GeoScience, 9302 Brookhurst Court, Tampa, FL 33647, USA.
E-mail address: pavel_k7@yahoo.com (P.K. Kepezhinskas).

https://doi.org/10.1016/j.oregeorev.2020.103800
Received 5 June 2020; Received in revised form 8 September 2020; Accepted 22 September 2020
Available online 25 September 2020

and Kelemen, 2019) and basaltic lavas (Evans et al., 2012; Brounce et al., 2014). This oxidation state is traditionally attributed to high water contents of subduction zone magmas (Kelley and Cottrell, 2009; Grove et al., 2012; Plank et al., 2013) and/or general aqueous (S- and C-bearing) fluid-fluxed nature of sub-arc mantle wedge (Grove et al., 2006; Birner et al., 2017; Iacovino et al., 2020). However, mantle wedge xenoliths from the Kamchatka arc (Kepezhinskas et al., 2002; Ishimaru et al., 2009) and chromitites in supra-subduction ophiolites (Yang et al., 2015; Zhang et al., 2016) contain native metals and metal alloys such as awaruite (Ni_2Fe) and kamacite (NiFe) suggesting existence of small-scale redox heterogeneity in sub-arc lithosphere. Recent studies of mantle wedge peridotites and deep arc cumulates in nascent arcs and fore-arc regions suggest that reduced conditions (oxygen fugacity values below the fayalite-magnetite-quartz buffer) may exist either during subduction initiation or during fractionation of primitive magmas at deeper levels in island-arc crust (Birner et al., 2017; Tang et al., 2018; Tao et al., 2020).

Chalcophile and siderophile elements occur as native metals and

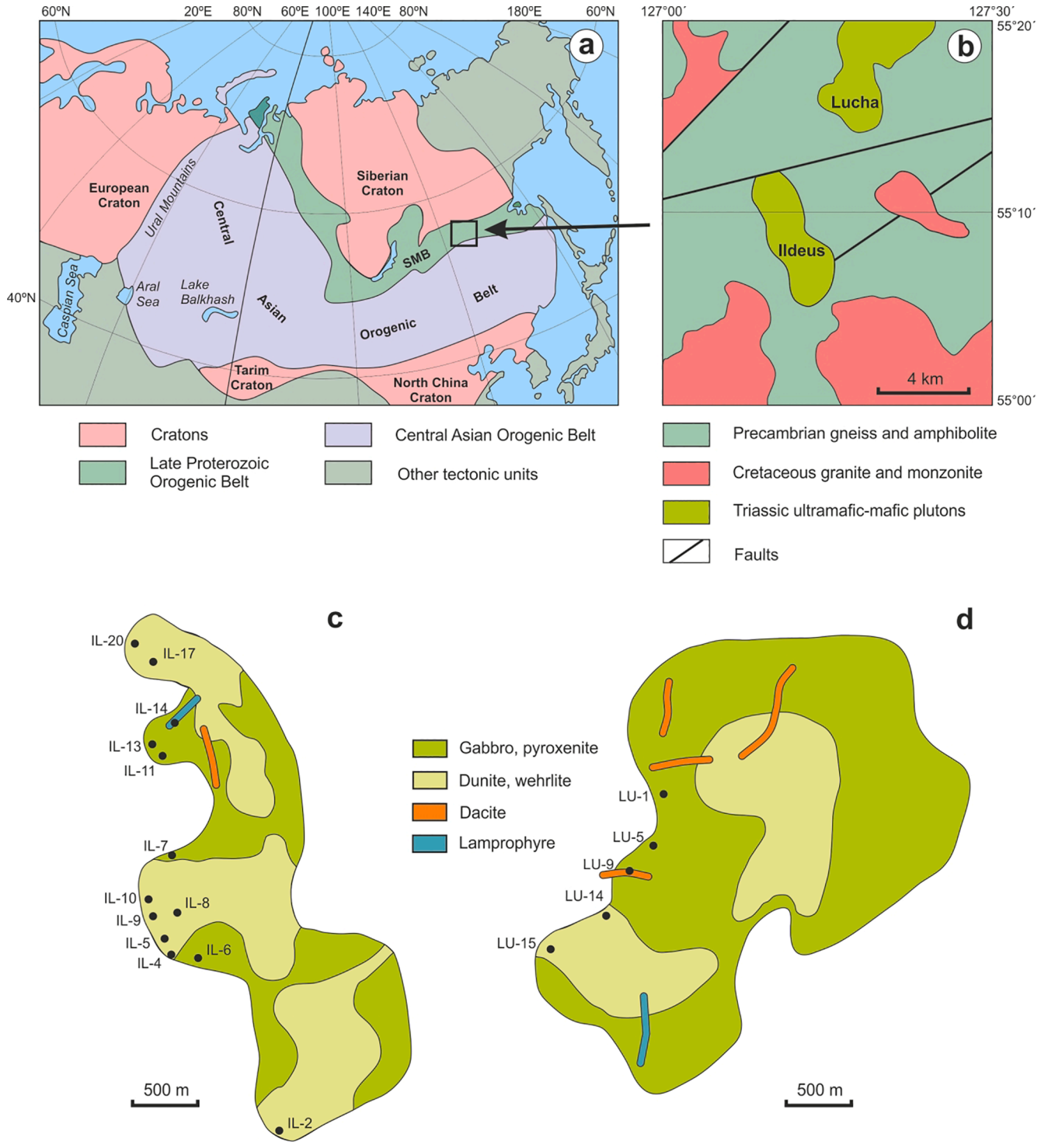

Fig. 1. General tectonic setting (a; after Kröner et al., 2014), regional geology (b), and simplified geologic maps of the Ildeus (c) and Lucha (d) intrusions with sample locations (Stanovoy mobile belt, Far East Russia).

intermetallic compounds in a variety of ultramafic-mafic assemblages such as layered intrusions (Chamberlain et al., 1965; Wernette et al., 2019), primitive Mg-rich magmas (Zhang et al., 2006), oceanic serpentinites (Früh-Green et al., 2004), orogenic peridotites (Lorand et al., 2010), Alpine-type serpentinized peridotites (Schwarzenbach et al., 2014; Sciortino et al., 2015) and mantle xenoliths (Kepezhinskas et al., 2002: Tassara et al., 2017). Petrologic constraints suggest that low-redox conditions are required for native metal formation in ultramafic-mafic rocks, possibly in the presence of reduced, hydrogen- and/or methane-rich fluids (Frost, 1985; Evans, 2008).

We present in this paper new mineralogical and geochemical evidence for the occurrence of native metals and intermetallic compounds in ultramafic rocks from the Ildeus-Lucha plutonic complex (ILC) in the Stanovoy mobile belt of Far East Russia. The ILC represents a long-lived (~100 Ma) crustal plumbing system with a complex magmatic to metamorphic evolution and distinct metal enrichments (Kepezhinskas et al., 2018, 2019). New data presented in this paper allow us not only to provide new information on a unique chalcophile and siderophile metal mineralization in a major orogenic setting, but also to shed some light on petrologic processes responsible for unusual redox heterogeneity within the subduction-related lithosphere.

2. Geologic setting

The Stanovoy mobile belt forms part of the Central Asian Orogenic Belt (CAOB), a continent-scale assortment of various Precambrian crustal fragments, oceanic and suprasubduction-type ophiolites, island arcs, oceanic islands, seamounts, oceanic plateaus, eclogite and blueschist belts (Kepezhinskas, 1986; Kepezhinskas et al., 1991; Safonova, 2017) amalgamated by voluminous granitoid magmatism (Jahn et al., 2000; Jahn, 2004; Kröner et al., 2014). The CAOB records a protracted history of Neoproterozoic to Mesozoic subduction and collision episodes resulting in nearly continuous continental crust production during the Phanerozoic (Sengör et al., 1993; Windley et al., 2007). Current geodynamic models view the CAOB as an ancient analogue of the modern Western Pacific and assign its formation to the closure of the Paleo-Asian Ocean, where multiple Precambrian microcontinents, oceanic basins and island arcs existed in the late Neoproterozoic to early Paleozoic (Windley et al., 2007).

From structural viewpoint, Stanovoy mobile belt (SMB) forms a major Proterozoic suture along the southern margin of the Siberian craton (Fig. 1a) thrust over the Archean high-grade complexes of the Aldan Shield in the Paleoproterozoic (Nutman et al., 1992; Vernikovsky et al., 2004). The Aldan-Stanovoy suture is composed of variably deformed fragments of granite-greenstone terranes, tonalite-trondhjemite-granite (TTG) complexes and various Archean (2.6–3.2 Ga) supracrustal rocks (Fig. 1b) metamorphosed in granulite facies (Perchuk et al., 1985; Nutman et al., 1992) and intruded by charnockitic granites (2.5–2.6 Ga; Kröner et al., 2014). Paleoproterozoic (1960–1910 Ma) volcanic-sedimentary rocks are metamorphosed in amphibolite facies (Fig. 1b) and amalgamated together with Archean granulites and TTGs at ~1.9 Ga (Nutman et al., 1992). The SMB was involved in the Neoproterozoic to Early Paleozoic active margin processes (Kröner et al., 2014) and later re-activated in the Early Mesozoic due to the development of Uda-Murgal-Stanovoy island arc system along the southern and southeastern margin of the Siberian craton (Parfenov et al., 1978; Didenko et al., 2010).

The SMB contains several ultramafic-mafic intrusions of Paleozoic to Mesozoic age (Fig. 1b). The Late Triassic (232–233 Ma) intrusive massifs of Ildeus (Fig. 1c) and Lucha (Fig. 1d) are zoned and composed principally of dunite-wehrlite cores and pyroxenite-gabbro rims impregnated by later-stage pyroxenite veins, dikes and small intrusions (Kepezhinskas et al., 2018). Later-stage pyroxenite intrusions in the ILC occasionally display discordant relationships with both dunite-wehrlite sequences and host Precambrian orthogneisses. Gabbro typically occurs as thin (several meters wide) slivers along tectonic and relic magmatic contacts between the Ildeus intrusion and host metamorphic rocks. Dunites and wehrlites in the ILC locally display crude zoning, mostly due to the varying content of plagioclase (Fig. 2a, d) and orthopyroxene, although mineral layering typical of ultramafic-mafic layered intrusions such as Bushveld and Skaergaard, is conspicuously lacking. Some wehrlites contain thin (several millimeters) veins and selvages composed primarily of orthopyroxene (Fig. 2c). Ultramafic-mafic rocks of the ILC underwent serpentinization and greenschist to amphibolite metamorphism (~140 Ma) followed by intrusion of Cretaceous (114–117 Ma) amphibole-biotite dacites and potassic lamprophyres (Kepezhinskas et al., 2018).

3. Analytical methods

Major element compositions of bulk rock samples were analyzed using a S4 Pioneer X-ray spectrometer on pressed pellets at the regional Center for Innovative Analytical Methods (CIAM, Khabarovsk, Russian Federation). All of the analytical data were normalized against international - LDI-3 (gabbro) and WMG-1a (mineralized gabbro) – as well as Russian – DVB (basaltic andesite), DVA (andesite) and DVD (dacite) – rock reference standards. Analytical uncertainty for major elements is ±10%. Trace element abundances of bulk rock samples were measured using an ELAN 9000 ICP-MS after an acid digestion of sample powders at the CIAM. The same set of rock reference standards (LDI-3, WMG-1a, DVB, DVA and DVD) along with Perkin Elmer standard solutions PE# N9300231-9300234 were used to monitor analytical accuracy. The accuracy was ±5% for the trace elements with abundances of >20 ppm and ±10% for elements with abundances of <20 ppm. Further details of analytical techniques used in this study are reported in Berdnikov et al. (2020).

Olivine and pyroxene compositions in the ILC rocks were obtained using a Cameca SX100 electron microprobe at the Central Science Laboratory, University of Tasmania (Hobart, Tasmania). Analytical conditions were 15 kV accelerating voltage, 30nA beam current and counting times of 10 to 40 s for different elements. Analyses were acquired using Kα lines and LLiF, LPET, PET and TAP analyzing crystals and a set of natural and synthetic standards were used as specified in Kamenetsky et al. (2016). Standard ZAF correction procedures were applied during data acquisition and processing.

Chemical compositions of other minerals and metallic phases were obtained using a VEGA 3 LMH TESCAN scanning electron microscope with the Oxford X-Max 80 (GB) EDS spectrometer (accelerating voltage −20 kV, beam current −530 pA, beam diameter −0.2 μm). A set of reference materials including 37 natural and synthetic oxides, minerals and metallic chemical elements (Oxford/108699 # 6067) was used as reference standards; Co-standard Oxford Instruments/143100 # 9864-15 was used for routine daily instrument calibration. Individual grains as well as polished sections and rough surfaces of rocks and ores were used for investigation by the SEM. Additional details of analytical procedures used in this study can be found in Berdnikov et al. (2020).

4. Petrology and geochemistry of ultramafic rocks

4.1. Petrography and textures

Dunites and plagioclase-bearing dunites are most abundant in the core of the ILC (Fig. 1c, d). These rocks are dark grey, medium to fine-grained rocks with hypidiomorphic-granular texture composed of olivine (~90 modal percent), clinopyroxene with Mg-number (100*Mg/Mg + Fe) of 75 (~5 modal percent) and (in plagioclase-bearing varieties) plagioclase (~5 modal percent). Amphibole with brown pleochrosim locally replaces clinopyroxene and is included in intercumulus plagioclase (Fig. 2d). Some plagioclase-bearing dunites exhibit cumulate texture with cumulus phases composed of olivine and pyroxene and intercumulus phases – of calcic plagioclase (Fig. 2a). Accessory phases include spinel, magnetite and sulfides (pentlandite, Co-pentlandite,

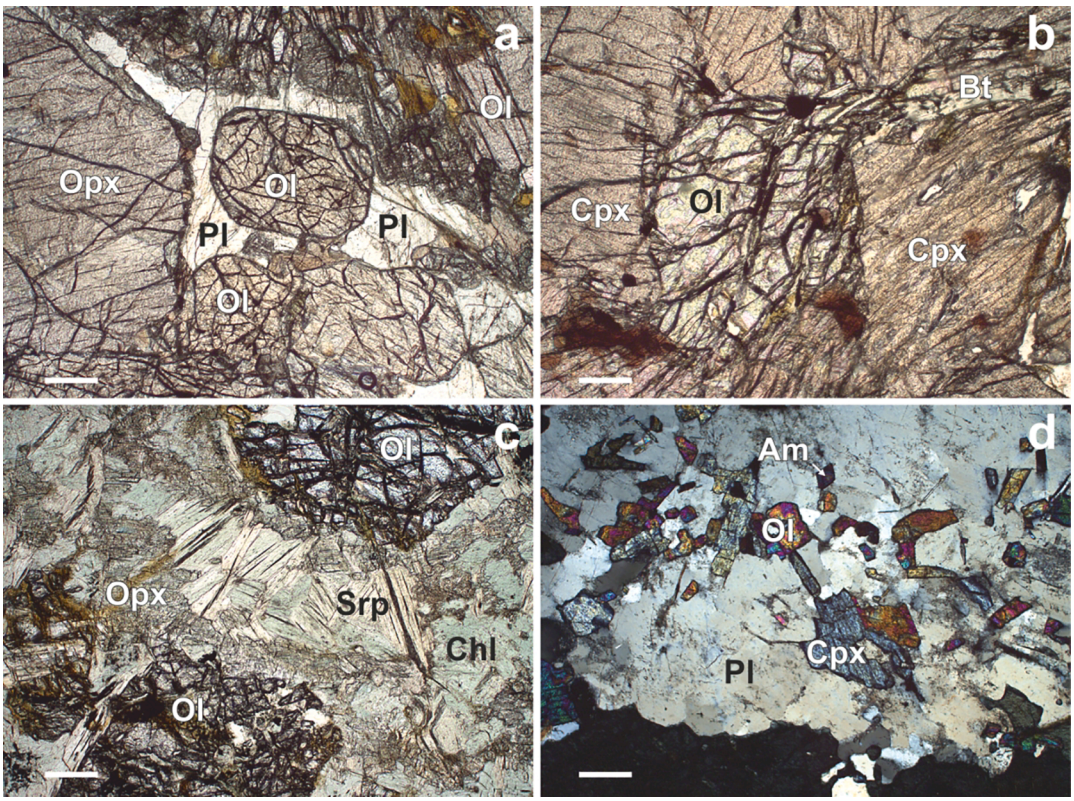

Fig. 2. Ultramafic and mafic rocks of the ILC: a) plagioclase-bearing dunite with cumulate texture; b) biotite-bearing wehrlite; c) pyroxenite veinlet in dunite; d) poikilitic texture of gabbro. Ol – olivine, Opx – orthopyroxene, Cpx – clinopyroxene, Am – amphibole, Bt – biotite, Pl – plagioclase, Chl – chlorite, Srp – serpentine. Scale bar in all photos – 20 μm.

chalcopyrite, nickeliferous pyrite and pyrrhotite). Secondary minerals include serpentine (mostly antigorite), chlorite, tremolite and actinolite. Serpentinization is frequently accompanied by formation of clusters and trails of secondary, fine-grained magnetite.

Wehrlites are dark green to brown grey massive rocks with granular and pseudomorphic net texture composed of olivine (up to 50 modal percent), clinopyroxene (up to 40 modal percent), orthopyroxene (up to 7 modal percent), plagioclase and rare biotite (Fig. 2b). Olivine forms euhedral to subhedral grains up to 1 mm in size. Clinopyroxene frequently forms large (up to 3 mm) oikocrysts, which contain numerous inclusions of olivine, orthopyroxene and earlier clinopyroxene. Orthopyroxene occurs as inclusions in large clinopyroxene oikocrysts, as well as euhedral to subhedral crystals frequently surrounded by serpentine-tremolite-chlorite aggregate. Anhedral plagioclase (0.1–0.7 mm) occasionally co-exists with interstitial biotite. Primary magnetite and spinel typically have interstitial appearance, while secondary magnetite occurs in serpentinized olivine and orthopyroxene. Other accessory minerals include pentlandite, chalcopyrite, bornite, sphalerite, ilmenite and apatite.

Pyroxenites in the ILC are composed of varying amounts of clinopyroxene (40–50 modal percent), orthopyroxene (40–50 modal percent), pargasitic amphibole and minor biotite (up to 10 modal percent combined). Secondary minerals are serpentine, actinolite and chlorite (Fig. 2c). Accessory phases include zircon, titanite, rutile, Cl-F-apatite, barite, Co- and Au-bearing pentlandite, bornite, millerite, heazlewoodite and digenite.

Mafic rocks are common along the margins of the ILC and at the tectonic contacts with host Precambrian gneisses and amphibolites (Fig. 1c and d). Gabbros and gabbro-norites typically have hypidiomorphic to poikilitic texture composed of variable amounts of clinopyroxene, orthopyroxene, plagioclase, olivine (in olivine gabbros), pargasitic hornblende and biotite (Fig. 2d). Secondary alteration of gabbroic rocks is quite variable, represented by tremolitic to actinolitic amphibole, chlorite, sericite, epidote as well as albite and clay minerals replacing plagioclase. Accessory minerals include magnetite (frequently with minor vanadium), titanite, zircon, apatite (including F-Cl-rich varieties), rutile and rare (La-Ce-Nd)-allanite.

4.2. Mineral chemistry

Olivines in dunites, wehrlites and pyroxenites exhibit a range of chemical compositions (Table 1), especially in respect to MgO (41.45–46.08 wt%), FeO (14.42–19.58 wt%), MnO (0.21–0.36 wt%) and NiO (0.16–0.31 wt%). Most olivines contain virtually no CaO, Al_2O_3, TiO_2 and, in most cases, Cr_2O_3 (0.00–0.01 wt%; Table 1). Orthopyroxenes classify as enstatites with elevated Al_2O_3 and TiO_2 contents (Table 1); clinopyroxenes classify as diopsides with elevated Al_2O_3 and Na_2O contents (Table 1).

4.3. Bulk-rock geochemistry

Major and trace element concentrations in rocks from the ILC are listed in Table 2. Cumulate ultramafics display generally low (<1 wt%) TiO_2 contents with the exception of pyroxenites IL-6 and IL-13 (1.42 and 1.20 wt% TiO_2, respectively; Table 2). All ultramafic rocks have elevated Al_2O_3 contents (dunites – 1.51–5.90 wt%, wehrlites – 3.31–8.59 wt%, pyroxenites – 4.76–15.15 wt%; Table 2) and variable MgO, Cr, Ni and Co contents (Table 2). Dunites exhibit rather high LOI contents (6.43–12.40 wt%), which correspond to high degrees of serpentinization. Concentrations of fluid-mobile, large-ion lithophile elements, such as Rb, Ba, Cs and U, are quite variable, while these of high-field strength elements (Nb, Ta, Zr) – appear to be uniformly low in respect to other incompatible elements (Table 2; Fig. 3a-d). Individual dunite samples are characterized by high Ba contents (569 ppm in IL-18 and 1456 ppm

Table 1
Representative compositions (wt. %) of olivines and pyroxenes from the Ildeus-Lucha complex.

Lithology	Dunite	Dunite	Dunite	Dunite	Dunite	Dunite	Dunite	Dunite	Dunite	Dunite
Sample N°	IL-9	IL-9	IL-9	IL-2	IL-2	IL-2	IL-2	IL-2	IL-2	IL-8
Mineral	Ol	Ol	Ol	Ol	Ol	Ol	Ol	Ol	Ol	Ol
SiO_2	39,15	39,24	39,19	40,05	39,94	39,79	39,51	39,72	39,70	39,47
TiO_2	0,00	0,00	0,00	0,00	0,01	0,00	0,00	0,00	0,01	0,00
Al_2O_3	0,00	0,01	0,00	0,01	0,00	0,01	0,00	0,00	0,01	0,00
Cr_2O_3	0,00	0,00	0,01	0,00	0,00	0,00	0,00	0,00	0,00	0,00
V_2O_3	0,01	0,01	0,01	0,01	0,01	0,01	0,01	0,00	0,01	0,01
FeO	18,69	18,57	18,90	15,24	14,71	14,94	15,33	14,86	14,70	15,98
MnO	0,25	0,26	0,24	0,23	0,22	0,25	0,27	0,23	0,21	0,27
MgO	42,21	42,35	42,46	45,72	45,68	45,44	45,29	45,41	45,34	44,15
CaO	0,00	0,01	0,01	0,00	0,00	0,00	0,01	0,01	0,01	0,00
NiO	0,25	0,26	0,24	0,24	0,28	0,26	0,23	0,28	0,23	0,30
ZnO	0,01	0,02	0,00	0,00	0,01	0,04	0,02	0,01	0,00	0,06
Na_2O	0,00	0,00	0,00	0,00	0,00	0,01	0,00	0,00	0,00	0,00
K_2O	0,00	0,00	0,00	0,00	0,00	0,00	0,00	0,01	0,00	0,00
Total	100,56	100,73	101,05	101,49	100,86	100,74	100,67	100,51	100,20	100,20
Lithology	Dunite	Dunite	Dunite	Dunite	Wehrlite	Wehrlite	Wehrlite	Dunite	Dunite	Wehrlite
Sample N°	IL-8	IL-8	IL-18	IL-18	IL-5	IL-5	IL-5	IL-9	IL-9	IL-5
Mineral	Ol	Ol	Ol	Ol	Ol	Ol	Ol	Opx	Opx	Cpx
SiO_2	39,42	39,37	38,74	39,16	39,03	39,15	39,27	54,73	53,59	51,24
TiO_2	0,01	0,01	0,00	0,00	0,00	0,01	0,00	0,13	0,18	0,91
Al_2O_3	0,00	0,01	0,01	0,00	0,00	0,02	0,02	2,97	3,66	5,66
$C_{r2}O_3$	0,00	0,00	0,00	0,00	0,00	0,01	0,00	0,12	0,30	0,42
V_2O_3	0,00	0,01	0,00	0,01	0,02	0,01	0,00	0,02	0,01	0,04
FeO	16,52	16,33	17,87	17,68	19,34	19,58	19,45	11,91	11,85	7,63
MnO	0,30	0,31	0,36	0,32	0,23	0,26	0,26	0,27	0,25	0,18
MgO	43,48	43,61	42,32	43,15	41,45	41,91	41,70	30,12	29,90	18,34
CaO	0,00	0,00	0,00	0,01	0,00	0,02	0,01	0,45	0,31	15,43
NiO	0,26	0,28	0,27	0,25	0,17	0,18	0,16	0,04	0,04	0,02
ZnO	0,00	0,05	0,04	0,04	0,00	0,02	0,00	0,01	0,00	0,00
Na_2O	0,00	0,01	0,00	0,00	0,00	0,01	0,00	0,02	0,01	0,78
K_2O	0,01	0,00	0,00	0,00	0,00	0,00	0,00	0,01	0,00	0,00
Total	99,76	99,95	99,60	100,61	100,20	101,17	100,82	100,81	100,09	100,60

in IL-13; Table 2), while some pyroxenites and gabbro display high Sr contents (466–1800 ppm; Table 2). Potassic (K_2O = 4.72 wt%; Table 2) magnesian (MgO = 13.78 wt%; Table 2) lamprophyre dike exhibits elevated Rb and Nb and, especially TiO_2 and Ba contents (3.36 wt% and 7035 ppm, respectively; Table 2; Fig. 3d). Amphibole-biotite dacite (Fig. 3d) displays high Sr (768 ppm) and, especially, Ba (2085 ppm) contents coupled with low Y (2.40 ppm) and Yb (0.17 ppm) contents as well as high Sr/Y ratio of 320 (Table 2). All ultramafic and mafic rocks in the ILC display depletions in high-field strength elements, such as Nb, Ta, Zr and Hf, and substantial variations in large-ion lithophile elements, such as Rb, Ba and U (Fig. 3a-d). Dunites and wehrlites from the ILC have chondrite-normalized rare earth patterns variably enriched in light rare earth elements (LREE), while pyroxenites exhibit LREE-enriched, subchondritic and LREE-depleted patterns (Fig. 3e-g). Marginal gabbro, biotite-amphibole dacite and potassic lamprohyre are moderately enriched in LREE and have weak positive Eu anomaly (Fig. 3h).

5. Native metals, intermetallic compounds and associated minerals

We summarize in this section textural occurrences and petrographic features of native metals, defined as naturally occurring zero valency metals, and intermetallic compounds (crystalline substances composed of definite proportions of two or more metals) as well as their associated minerals (halogen- and REE-bearing minerals, oxides, sulfates, sulfides, sulfosalts, phosphates and carbonates). Native (zero valency) metals (W, Pt, Au, Ag, Zn, Bi) and intermetallic compounds (platinum group metals, copper-silver-gold, copper-tin-zinc and antimony-lead) were documented in 14 ultramafic samples from the ILC. Representative occurrences are summarized in Table 3 and presented in Figs. 4–7.

5.1. Native metals

Native metals are typically observed as inclusions in primary (magmatic) and secondary (metamorphic and metasomatic) silicate minerals, or grains in the interstitial matrix (Table 3). Tungsten occurs as single anhedral crystals (1–5 μm) included in high-Ni, low-Mn olivine (Fig. 4a). Tungsten particles are completely enclosed in olivine grains with no evidence for later-stage origins, such as crack sealing or localization inside secondary cavities.

Euhedral platinum grains (2–3 μm in size) are included in clinopyroxene (Fig. 4b) and Cr-tremolite (Cr_2O_3 = 0.58 wt%) replacing clinopyroxene. Platinum is also associated with Cr-magnetite (9–11 wt% of Cr_2O_3) in the interstitial matrix between larger olivine and orthopyroxene grains.

Gold and silver are the most abundant native metal phases in the ILC (Table 3). Gold occurs as inclusions (2–30 μm) in orthopyroxene porphyroclasts and fine-grained orthopyroxene aggregates, olivine, clinopyroxene, biotite, amphibole (Fig. 4c), tremolite and chlorine-bearing (Cl = 0.14 wt%) chlorite. Gold is also found as discrete grains in fine-grained interstitial matrix composed principally of amphibole, sericite and serpentine. Some gold particles are localized along the boundaries of olivine, clinopyroxene, orthopyroxene, plagioclase, amphibole and biotite grains. In several cases, gold occurs near larger crystals of V-bearing, Cr-rich magnetite and Ti-magnetite. All gold contains silver (0.5–15.62 wt%) in addition to iron (1.91 wt%), zinc (3.21–4.38 wt%) and copper (3.72–4.77 wt%).

Native silver occurs as subhedral to anhedral inclusions (1–25 μm) in low-Ca olivine, orthopyroxene, pargasitic amphibole, tremolite, chlorite (Fig. 4d), Cl-bearing biotite and Cl-bearing serpentine. Most silver grains contain some zinc (0.8–2.76 wt%) and copper (1.92–4.83 wt%). Some silver inclusions in olivine, orthopyroxene and chlorite are rimmed by chalcopyrite. One anhedral silver particle (10 μm) with high copper

Table 2
Representative analyses (major oxides - wt.%, trace elements - ppm) of ultramafic–mafic rocks from the Ildeus-Lucha complex.

Intrusion	Ildeus									
Rock type	Dun	Dun	Dun	Dun	Dun	Dun	Wehr	Wehr	Wehr	
Sample N°	IL-2*	IL-18	IL-8	IL-9	IL-10	IL-20	IL-17	IL-4	IL-5	
SiO_2	33,30	38,30	39,09	39,35	39,52	38,16	49,03	44,05	48,07	
TiO_2	0,03	0,14	0,14	0,11	0,14	0,18	0,23	0,39	0,49	
Al_2O_3	1,51	5,90	4,70	5,41	1,85	3,30	3,31	5,28	5,50	
Fe_2O_3	12,20	9,36	10,97	10,45	11,70	12,04	9,65	13,09	12,59	
MnO	0,16	0,17	0,17	0,15	0,17	0,19	0,16	0,20	0,21	
CaO	0,34	1,15	1,36	1,73	0,62	0,25	1,20	3,58	2,72	
MgO	38,50	33,07	33,09	33,21	38,60	33,65	31,00	27,20	27,72	
Na_2O	0,02	0,18	0,20	0,21	0,19	0,12	0,16	0,63	1,17	
K_2O	0,03	0,03	0,04	0,06	0,02	0,03	0,02	0,05	0,09	
P_2O_5	0,01	0,03	0,03	0,03	0,04	0,03	0,02	0,03	0,04	
LOI	12,40	11,98	10,24	9,26	6,43	12,01	5,18	5,01	0,76	
Total	98,50	100,33	100,02	99,96	99,28	99,96	99,97	99,50	99,36	
Li	n.d.	1,23	1,26	1,51	1,28	0,36	0,33	1,08	1,41	
Sc	5	10,74	8,52	7,76	6,03	12,40	21,59	20,42	24,52	
V	23	56,23	44,12	43,98	21,38	82,14	94,23	91,28	103,39	
Cr	3370	2322,37	2648,89	2641,12	643,17	4711,17	2645,22	2039,36	1741,42	
Co	147	108,16	111,96	102,04	126,54	164,28	74,11	102,95	74,25	
Ni	2100	1605,18	1772,76	1541,28	1903,48	2516,41	885,88	999,96	733,76	
Cu	116	44,57	67,47	79,43	29,26	24,31	8,62	51,44	104,33	
Zn	92	96,88	84,49	80,35	24,71	132,46	91,10	76,93	48,74	
Se	0,3	<0.001	<0.001	<0.001	0,05	<0.001	<0.001	<0.001	<0.001	
Rb	0,6	0,61	0,70	1,50	0,29	0,31	0,22	0,65	0,88	
Sr	13,4	48,26	55,29	99,08	37,84	9,30	13,61	105,34	150,26	
Y	0,5	3,22	2,11	2,02	1,69	2,50	3,17	5,54	5,77	
Zr	2	12,11	0,99	1,85	4,99	19,74	1,69	6,43	14,39	
Nb	0,2	0,76	0,05	0,19	0,10	0,58	0,02	0,28	0,47	
Te	0,03	<0.001	<0.001	<0.001	<0.001	<0.001	<0.001	<0.001	<0.001	
Cs	0,01	0,07	0,04	0,06	0,01	0,01	0,00	0,12	0,08	
Ba	16,7	569,72	48,73	55,99	22,73	71,64	39,99	107,18	66,81	
La	0,5	2,71	1,19	1,17	0,83	1,67	0,74	1,18	1,77	
Ce	0,6	6,22	2,77	2,54	1,91	6,87	2,58	3,89	4,39	
Pr	0,07	0,62	0,35	0,33	0,26	0,44	0,26	0,57	0,59	
Nd	0,2	2,42	1,59	1,46	1,16	1,75	1,32	2,99	2,76	
Sm	0,05	0,54	0,38	0,34	0,28	0,42	0,39	0,85	0,75	
Eu	0,03	0,25	0,16	0,15	0,09	0,12	0,11	0,33	0,28	
Gd	0,06	0,69	0,47	0,42	0,35	0,55	0,52	1,10	1,01	
Tb	0,01	0,10	0,07	0,06	0,05	0,08	0,08	0,17	0,16	
Dy	0,06	0,63	0,40	0,38	0,30	0,48	0,55	1,04	1,02	
Ho	0,02	0,13	0,08	0,08	0,06	0,10	0,12	0,22	0,22	
Er	0,04	0,38	0,23	0,22	0,18	0,28	0,36	0,62	0,67	
Tm	n.d.	0,06	0,03	0,03	0,02	0,04	0,05	0,09	0,10	
Yb	0,08	0,38	0,22	0,22	0,18	0,28	0,34	0,56	0,67	
Lu	n.d.	0,06	0,03	0,03	0,03	0,04	0,05	0,08	0,11	
Hf	0,2	0,42	0,05	0,04	0,10	0,25	0,04	0,25	0,41	
Ta	0,1	0,33	0,02	0,02	<0.001	0,01	<0.001	0,16	0,09	
Pb	2	1,40	0,68	1,17	1,19	0,74	1,46	1,36	4,10	
Th	0,05	0,35	0,04	0,20	0,03	0,31	0,03	0,30	0,25	
U	0,05	3,33	0,81	1,64	1,53	3,15	<0.001	1,78	1,82	

Intrusion	Ildeus				Lucha				Later-stage dikes	
Rock type	Pyr	Pyr	Pyr	Pyr	Wehr	Wehr	Pyr	Gab	K-Lamp	Dac
Sample N°	IL-6	IL-7	IL-11	IL-13	LU-15	LU-14	LU-5	LU-1	IL-14	LU-9
SiO_2	49,48	48,29	44,47	47,34	41,05	42,39	48,42	50,12	44,21	68,85
TiO_2	1,42	0,47	0,37	1,20	0,17	0,16	0,56	0,99	3,36	0,09
Al_2O_3	4,76	6,32	15,15	10,51	8,32	8,59	5,74	16,94	13,11	15,42
Fe_2O_3	15,48	13,27	7,74	12,55	9,57	10,12	11,88	9,73	13,22	1,31
MnO	0,25	0,22	0,13	0,17	0,14	0,14	0,18	0,13	0,11	0,04
CaO	4,14	6,26	9,57	4,07	3,75	1,97	9,71	7,39	1,24	1,06
MgO	20,83	21,88	15,21	15,65	27,99	28,32	20,15	6,73	13,78	1,36
Na_2O	0,63	1,34	5,72	3,12	0,42	0,36	1,01	5,79	2,78	7,11
K_2O	0,06	0,06	0,30	2,49	0,06	0,16	0,06	0,33	4,72	3,62
P_2O_5	0,02	0,01	0,01	0,78	0,08	0,04	0,03	0,31	0,08	0,04
LOI	2,58	1,26	1,12	1,60	8,48	7,76	1,99	1,54	1,93	0,55
Total	99,65	99,38	99,81	99,49	100,01	99,81	99,09	99,79	98,54	99,45
Li	1,85	1,07	4,11	6,96	1,61	2,47	4,02	5,20	18,69	2,68
Sc	37,26	25,58	26,63	12,99	7,44	14,29	54,62	16,75	5,72	1,92
V	327,22	105,15	94,86	116,74	29,42	59,07	208,08	143,80	229,24	8,12
Cr	1257,15	1920,24	1032,86	414,57	465,04	1463,54	1424,09	130,29	269,18	74,42
Co	81,42	52,81	43,71	62,83	73,96	85,75	43,00	31,14	56,50	10,90
Ni	473,86	435,50	465,75	298,28	519,58	701,34	452,05	80,05	193,16	43,11
Cu	25,59	113,81	36,23	64,77	18,39	64,90	75,75	30,00	30,06	42,86

(*continued on next page*)

Table 2 (*continued*)

Intrusion	Ildeus									
Rock type	Dun	Dun	Dun	Dun	Dun	Dun	Wehr	Wehr	Wehr	
Sample N°	IL-2*	IL-18	IL-8	IL-9	IL-10	IL-20	IL-17	IL-4	IL-5	
Zn	109,39	56,38	64,93	166,05	78,27	89,35	55,08	95,66	404,41	130,83
Se	<0.001	<0.001	<0.001	<0.001	<0.001	<0.001	<0.001	<0.001	<0.001	<0.001
Rb	0,67	0,46	5,67	32,73	1,70	5,19	0,28	2,40	81,14	26,00
Sr	30,88	179,55	1800,71	466,10	58,42	39,95	30,09	1452,68	477,02	768,44
Y	8,63	5,46	7,84	19,80	4,63	4,34	12,42	7,91	2,23	2,40
Zr	4,07	10,19	9,37	8,80	3,71	4,23	3,51	4,78	4,44	10,58
Nb	0,27	0,11	0,14	1,13	0,53	0,45	<0.001	0,36	10,69	1,26
Te	<0.001	<0.001	<0.001	<0.001	<0.001	<0.001	0,06	<0.001	<0.001	<0.001
Cs	0,04	0,03	0,35	0,53	0,13	0,18	0,02	0,11	1,18	0,25
Ba	36,37	95,12	232,92	1456,81	69,11	125,22	5,90	330,14	7035,78	2085,29
La	1,10	1,01	1,67	37,12	3,52	2,23	0,59	9,74	4,91	2,10
Ce	3,87	2,59	4,48	79,06	8,19	5,35	2,59	21,53	9,38	4,59
Pr	0,65	0,39	0,73	9,41	1,08	0,71	0,57	2,83	1,02	0,57
Nd	3,92	2,05	3,97	36,16	4,65	2,96	3,68	12,42	3,73	2,21
Sm	1,31	0,60	1,23	6,32	1,06	0,74	1,49	2,61	0,66	0,52
Eu	0,55	0,27	0,70	2,08	0,35	0,19	0,55	1,30	0,47	0,27
Gd	1,66	0,84	1,59	6,46	1,19	0,93	2,15	2,79	0,67	0,58
Tb	0,27	0,14	0,25	0,77	0,17	0,15	0,39	0,36	0,07	0,09
Dy	1,64	0,94	1,51	3,84	0,96	0,86	2,46	1,77	0,39	0,46
Ho	0,34	0,21	0,31	0,71	0,19	0,18	0,53	0,33	0,07	0,09
Er	0,98	0,66	0,84	1,96	0,54	0,51	1,47	0,86	0,21	0,21
Tm	0,14	0,10	0,11	0,25	0,08	0,08	0,21	0,11	0,02	0,03
Yb	0,92	0,68	0,69	1,51	0,50	0,47	1,30	0,67	0,17	0,17
Lu	0,14	0,10	0,10	0,22	0,08	0,07	0,20	0,10	0,02	0,02
Hf	0,22	0,28	0,36	0,47	0,16	0,12	0,29	0,28	0,11	0,40
Ta	0,06	0,06	0,11	0,11	0,05	0,10	<0.001	0,05	0,41	0,03
Pb	0,81	0,94	12,01	3,24	2,23	1,64	17,46	6,21	5,24	35,86
Th	0,12	0,04	0,02	2,54	2,01	0,52	0,00	0,23	1,03	0,36
U	1,12	1,10	0,57	0,69	1,03	1,65	2,16	2,34	1,45	1,95

Notes: *- analysis by the Acme Laboratories (Canada). N.d. - not determined. Dun - dunite, Wehr - wehrlite, Pyr - pyroxenite, Gab - gabbro, K-Lamp - K-lamprophyre, Dac – Dacite.

content (5.95 wt% Cu) is contained within a grain of Cr-rich (Cr_2O_3 = 2.94 wt%) magnetite (0.2 mm), which is, in turn, included in large mica porphyroclast. Other minerals associated with native silver in ILC rocks are cerargyrite and nickeliferous pyrite (Table 3).

Anhedral to subhedral zinc (2–2.5 μm) is included in amphibole (Fig. 4e) and observed as secondary-textured micro-particles in association with Na-, K- and Fe-chlorides inside a triangular-shaped indentation (measuring 40 μm across) in low-Ni, high-Mn olivine (Fig. 9c). Other inclusions in this olivine grain, located alongside the triangular crack, are pentlandite (1 μm) and magnetite (10 μm) (e.g. Fig. 9c).

Bismuth forms small (under 5 μm) partially resorbed grains or clusters of smaller particles included in orthopyroxene (Fig. 4f) and pargasitic amphibole (Table 3).

5.2. Compounds of platinum-group metals

Several anhedral grains of Pt-Fe alloys ranging in size from 1 to 5 μm occur as inclusions in primary orthopyroxene (Fig. 5a) and olivine (Table 3). A single discrete grain of subhedral nickeliferous (Ni = 1.8 wt %) rhodium-platinum compound (2.5 μm) is hosted in a fine-grained olivine-biotite-chlorite aggregate (Fig. 5b). A single subhedral grain of Pd-bearing platinum (3 μm) was identified inside a 3–5 μm-wide crack in orthopyroxene partially replaced by tremolite (Fig. 5c).

5.3. Copper-gold-silver compounds

Copper-gold-silver compounds are quite abundant and are hosted in various primary and secondary silicate minerals as well as oxides (Table 3). Euhedral to anhedral copper-silver compounds occur in orthopyroxene (Fig. 5d) in partially serpentinized peridotites. A subhedral cupriferous silver inclusion (15–17 μm) is associated with silver chloride with very thin NaCl film within a system of fissures in larger orthopyroxene grain (Fig. 5e). Parallel fissures in the same orthopyroxene grain are filled with chalcopyrite with variable Ni content (Fig. 5e). Other phases associated with copper-gold-silver compounds include copper-bearing acanthite or another, compositionally similar copper-silver sulfide (Fig. 5f). Some larger (100–200 μm) grains of Ag-Cu-Au compounds were recovered from crushed and washed out samples of ultramafic rocks from the ILC (Fig. 6a). Typically such alloys have euhedral or partially abraded

appearance and are characterized by Au:Cu ratios close to 2:1 (e.g. Fig. 6a). Euhedral to anhedral Ag-Cu-Au microparticles (<5 μm) occur in amphibole (Fig. 6b), biotite, chlorite and along the grain boundaries between Mn-rich olivine and orthopyroxene (not shown here). Large (typically greater than 20 μm) and small (<10 μm) grains of copper-gold-silver compounds display detectable compositional differences when plotted on a Cu-Au-Ag triangular diagram (Fig. 6c). In general, smaller grains tend to be enriched in gold in comparison with the larger particles (Fig. 6c).

In addition, gold, copper and silver form compounds with nickel and zinc. An elongated particle of Ag-Ni-Zn-Cu-Au composition is observed in amphibole (Fig. 6d), while still retaining typical Au:Cu ratio of 2:1. Silver-dominated compounds with zinc and copper are hosted in olivine-orthopyroxene aggregates (Fig. 6e) and native gold compounds with minor zinc and copper are occasionally included in orthopyroxene partially replaced by amphibole and chlorite (Fig. 6f).

5.4. Compounds of chalcophile metals

Copper frequently forms compounds with tin (natural bronzes) and zinc (natural brasses) in ultramafic rocks from the ILC (Table 3). Natural bronzes occur as anhedral, partially resorbed inclusions (3–20 μm) in clinopyroxene, amphibole (Fig. 7a), tremolite and biotite with compositions ranging from $Cu_{94}Sn_6$ to $Cu_{67}Sn_{33}$ (Fig. 7c). Tin-copper compounds in the ILC overlap (Fig. 7c) the compositional range of Sn-Cu metallic sublimates reported from the vesicle walls in basalts from Stromboli volcano (Hunter et al., 2020). Some tin-copper compounds in the ILC are associated with euhedral millerite (20–30 μm) included in

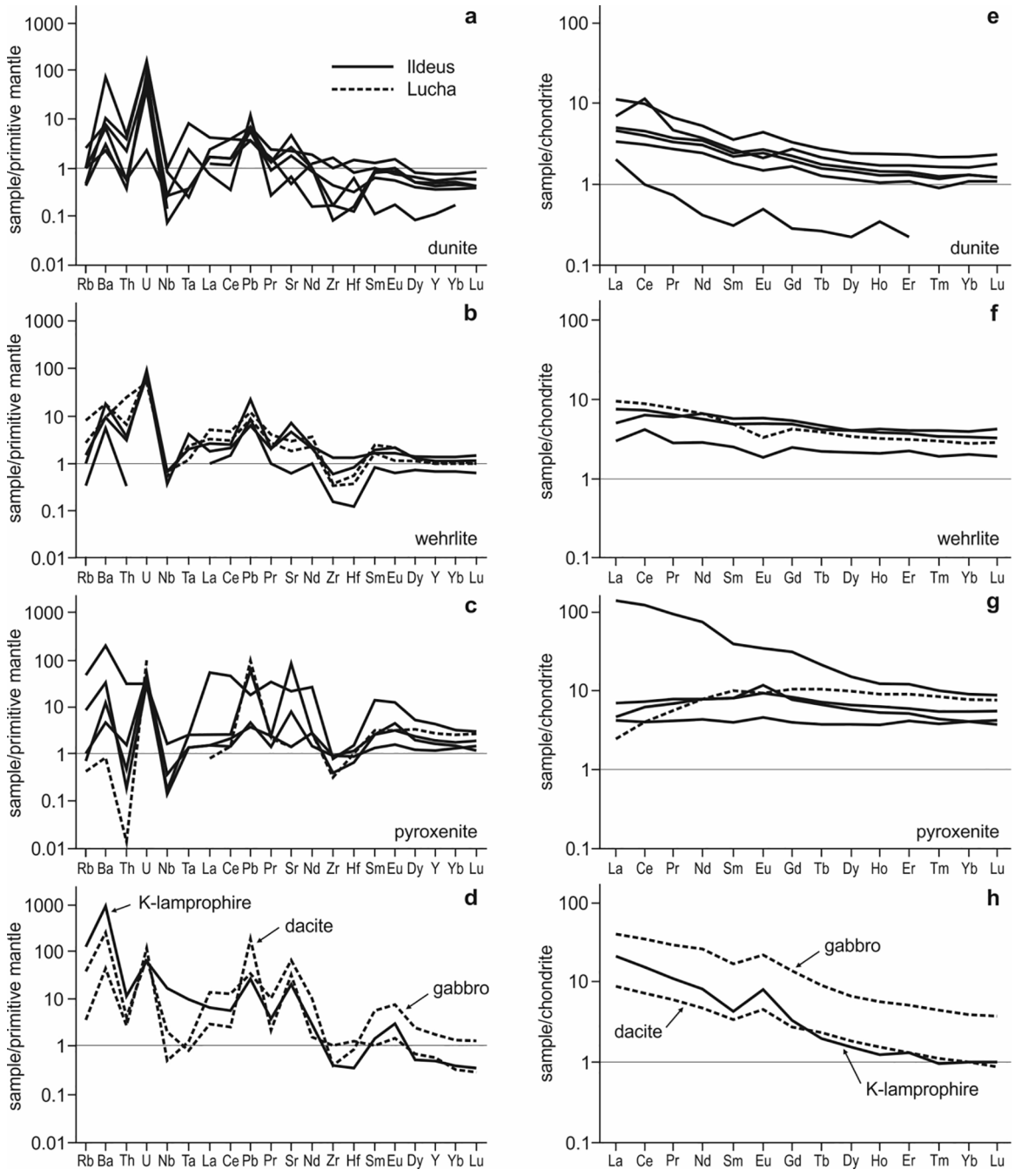

Fig. 3. Incompatible (a-d) and rare earth (e-h) element variations in ultramafic–mafic rocks from the Ildeus-Lucha complex and associated dikes normalized to primitive mantle and C1 chondrite, respectively (Sun and McDonough, 1989). (a and e) dunite and plagioclase-bearing dunite; (b and f) wehrlite and plagioclase-bearing wehrlite; (c and g) pyroxenite (including websterite); (d and h) gabbro, biotite-hornblende dacite and mica-rich potassic lamprophyre.

large (40–80 μm) grains of slightly porous Se-Cu-Ag-bearing altaite (Fig. 7d).

Zinc-copper compounds in the ILC ultramafics form relatively small (2–15 μm), resorbed isometric (occasionally roundish) inclusions in olivine (Fig.), clinopyroxene, amphibole and chlorite in association with ilmenite and Mg-Cr-Fe-Al-spinel (Table 3). Most natural brasses contain minor tin and form (with an exception of a single Cu-rich grain) a coherent compositional cluster on a triangular Sn-Cu-Zn diagram (Fig. 7c).

A single euhderal grain (5 μm) of a lead-antimony compound occurs as an inclusion in secondary (metasomatic) amphibole replacing clinopyroxene in wehrlite (Fig. 7f). The lead-copper compound is associated (in the same amphibole crystal) with large (~40 μm) grain of millerite containing small (~5 μm) particle of unidentified copper-lead sulfide (Fig. 7e).

5.5. Halogen- and REE-bearing mineral phases, oxides and sulfates

Halogen-bearing mineral phases, such as various halides, are common in the ILC ultramafic rocks (Table 3). In addition, some secondary-textured silicate phases (amphibole, biotite, serpentine, chlorite) contain variable amounts of chlorine. F-Cl-bearing apatites (frequently in association with chlorine-bearing amphibole, rutile, titanite and allanite) are common in metasomatized pyroxenites and gabbros (Table 4). Apatite typically occurs as subhedral, subequant to slightly elongated (rarely prismatic) crystals included, together with ilmenite,

Table 3
Summary of native metals and intermetallic compounds in ultramafic rocks from the Ildeus-Lucha complex.

Metals or intermetallic compounds	Number of grains identified	Associated minerals
Native metals		
Tungsten	6	Olivine, amphibole, orthopyroxene, ilmenite
Bismuth	2	Orthopyroxene, pargasitic amphibole
Zinc	2	Olivine, serpentine, tremolite, pentlandite, magnetite, halite (NaCl), Fe-hydroxides
Platinum	2	Cr-diopside, Cr-tremolite, Cr-magnetite, serpentine, chlorite
Gold	>50	Olivine, orthopyroxene, chlorite, Cl-bearing chlorite, clinopyroxene, serecite, amphibole, serpentine, plagioclase, V-Cr-magnetite, digenite, heazlewoodite
Silver	>30	Chlorite, ortopyroxene, olivine, amphibole, Ni-pyrite, serpentine, Cl-bearing serpentine, tremolite, digenite, chalcopyrite, Ag with Cl, NaCl (halite), Cr-magnetite, barite, Cl-biotite
Intermetallic compounds		
Cu-Ag-Au	19	Biotite, amphibole, olivine, orthopyroxene, chlorite, barite, apatite, titanite, rutile, ilmenite, allanite, quartz
Cu-Ag	7	Olivine, orthopyroxene, Cr-magnetite, serpentine, chalcopyrite, Ni-chalcopyrite, barite, Cu-bearing acanthite
Ni-Cu-Zn-Ag-Au	2	Amphibole, orthopyroxene, chlorite
Cu-Zn-Ag	3	Orthopyroxene, olivine
Cu-Zn-Au	2	Amphibole, orthopyroxene, chlorite, serpentine
Cu-Sn	12	Amphibole, tremolite, clinopyroxene, biotite, millerite, Cu-Ag-bearing altaite
Cu-Zn-Sn	9	Olivine, clinopyroxene, amphibole, serpentine
Pb-Sb	1	Amphibole, digenite, millerite, Cu-Pb-sulfide, Sb-Pb with Cl
Fe-Pt	3	Olivine, orthopyroxene
Ni-Rh-Pt	1	Olivine, biotite, chlorite, serpentine
Pd-Pt	1	Orthopyroxene, tremolite

rutile and allanite, in biotite (Fig. 8a) and amphibole (Fig. 8c). Apatite and the Fe-Ti-oxide-allanite are associated with plagioclase and quartz in some pyroxenites (Fig. 8c). Fe-Ti oxides frequently form euhedral to

Subhedral grains (>50 μm), which exhibit complex zoning patterns. Rutile cores (volumetrically dominant) are surrounded by reaction zone composed of finer-grained rutile-Ti-magnetite-titanite aggregate rimmed, in turn, by coarse ilmenite (Fig. 8b). Host minerals are usually olivine and orthopyroxene, with or without plagioclase (e.g. Fig. 8b). Titanite occurs in large (>1 mm) porphyroblastic amphibole grains along with pools of feldspathic material and vermicular plagioclase as well as clusters of equant K-halide (Fig. 8d).

Chlorine is present in a single anhedral grain of silver (6 μm) included in orthopyroxene (Fig. 9a), as well as in an euhedral, equant (3 μm) antimony-lead compound hosted in chlorite (Fig. 9b). Micro-particles and thin films (1–3 μm) of halite (NaCl) are present in association with pentlandite, subhedral magnetite (20 μm) and native zinc in large (~50 μm) triangular fissure in olivine (Fig. 9c). Micro-particles (2–5 μm) of Cl-rich (1.9–2.7 wt%) amphibole were detected as inclusions in olivine from

partially serpentinized dunite (Kepezhinskas et al., 2018). Finally, a single micro-particle of Ca-Mg bromide was observed together with V-Cr-bearing magnetite as inclusion in pargasitic amphibole (Kepezhinskas et al., 2019).

Barite is present in later-stage pyroxenites and gabbros (Table 3). Barite forms either equant clusters of subhedral grains in amphibole (Fig. 9d) and clinopyroxene, or vermicular (in cross-section, occasionally micro-folded) platy grains, which roughly follow plastic deformation structures in orthopyroxene (Fig. 9e) and olivine. Some magnetite grains included in orthopyroxene, amphibole and clinopyroxene exhibit thin (2 to 10 μm) rims of fibrous to polycrystalline barite (Fig. 9f). Barite is also observed as small (<10 μm) equant grains included in biotite or mixed together with finer-grained interstitial biotite-dominated matrix.

5.6. Associated Sulfides, sulfosalts and carbonates

Besides halogen-bearing minerals, native metals and intermetallic compounds in the ILC are associated with various sulfides, sulfosalts, and carbonates (Table 3). Disseminated sulfides are present in all studied samples of ultramafic–mafic rocks. Most common sulfides are pentlandite and Co-pentlandite (0.4–16 wt% of Co), chalcopyrite (nickeliferous chalcopyrite), bornite and pyrite with rare occurrences of

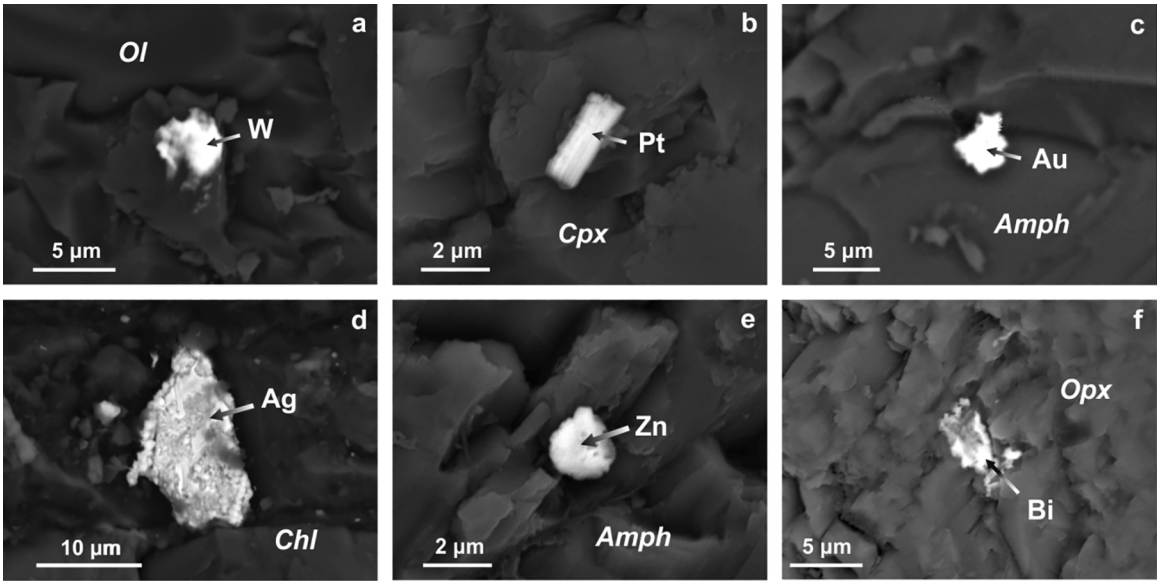

Fig. 4. SEM images of native metal inclusions in silicate minerals. a) tungsten (W) in olivine (Ol); b) platinum (Pt) in clinopyroxene (Cpx); c) gold (Au) in amphibole (Amph); d) silver (Ag) in chlorite (Chl); e) zinc (Zn) in amphibole (Amph); f) bismuth (Bi) in orthopyroxene (Opx).

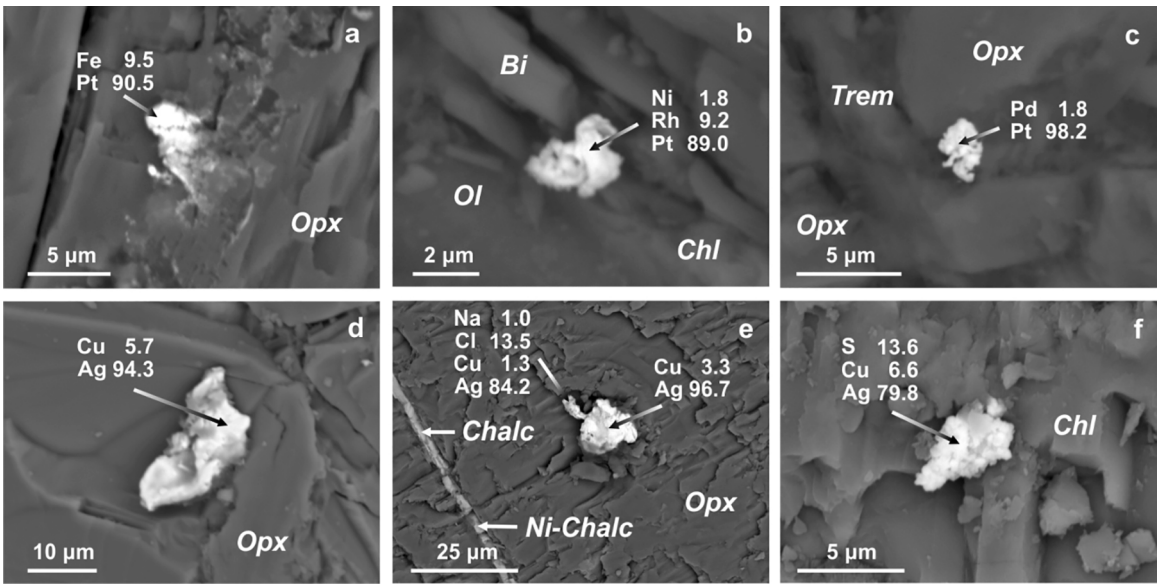

Fig. 5. Inclusions of precious metal compounds in silicate minerals from the ILC. a) ferroplatinum; b) nickel-rhodium-platinum; c) palladium-platinum; d) copper-silver; e) copper-silver with halite (NaCl); f) copper-bearing acanthite (?). Ol- olivine, Bi- biotite, Opx- orthopyroxene, Trem- tremolite, Chalc- chalcopyrite, Ni-Chalc- nickeliferous (Ni = 0.8 wt%) chalcopyrite.

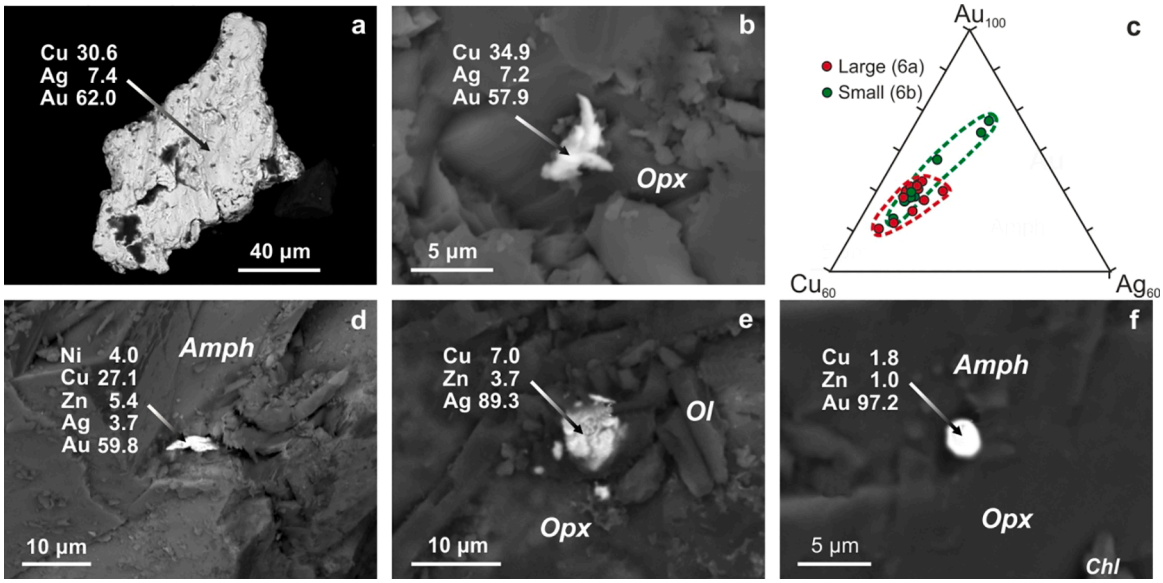

Fig. 6. SEM images of precious metals compounds with copper (a, b, d-f) and their compositional variations (c). a) and b) silver-copper–gold; c) compositional variations of Ag-Cu-Au compounds (large – >20 μm, small – <10 μm); d) copper–gold with minor silver, nickel and zinc; e) cupriferous silver with minor zinc; f) silver with minor zinc and copper. Opx – orthopyroxene, Ol – olivine, Amph – amphibole, Chl – chlorite.

nickeliferous pyrite, sphalerite, nickeliferous sphalerite, heazlewoodite, digenite, millerite (Fig. 7d, e) and unidentified copper-lead sulfide (Fig. 7e). Sulfosalts in the ILC rocks include gersdorffite, gratonite and arsenopyrite. A single grain of calcite with detectable concentrations of Br and Mn (0.4–0.5 wt% of each element) was found included in large Cr-magnetite.

6. Discussion

6.1. Tectonic setting and crustal evolution of the ILC

Ultramafic-mafic rocks from the ILC possess mineralogical (ubiquitous orthopyroxene, presence of intercumuls plagioclase, relatively early crystallization of high-Al pargasitic amphibole) and geochemical (high-Al and low-Ti, bulk-rock chemical character coupled with well-defined depletions in high-field strength elements; Fig. 3a-d; Table 2) characteristics typical of subduction-related igneous suites. Plutonic rocks of the ILC plot into the field of arc ultramafic and mafic cumulates on the AFM diagram (Fig. 10a) and display major -element variations observed in ultramafic–mafic plutons emplaced in other subduction environments such as Alaska (DeBari and Coleman, 1989), Kamchatka (Kepezhinskas et al., 1993) and the Cascades (Snoke et al., 1981). The ILC rocks exhibit very low Nb/Th ratios typical of island-arc basalts (Ryerson and Watson, 1987; Hochstaedter et al., 2001; Kent and Elliott, 2002) and plot into the arc field on the Zr/Nb-Nb/Th discrimination graph (Fig. 10b). Typically, Nb is fractionated from other fluid-immobile elements (such as Th and LREE) in subduction-related magmas (Pearce and Peate, 1995; Elliott et al., 1997; Kerrich and Xie, 2002), allowing for

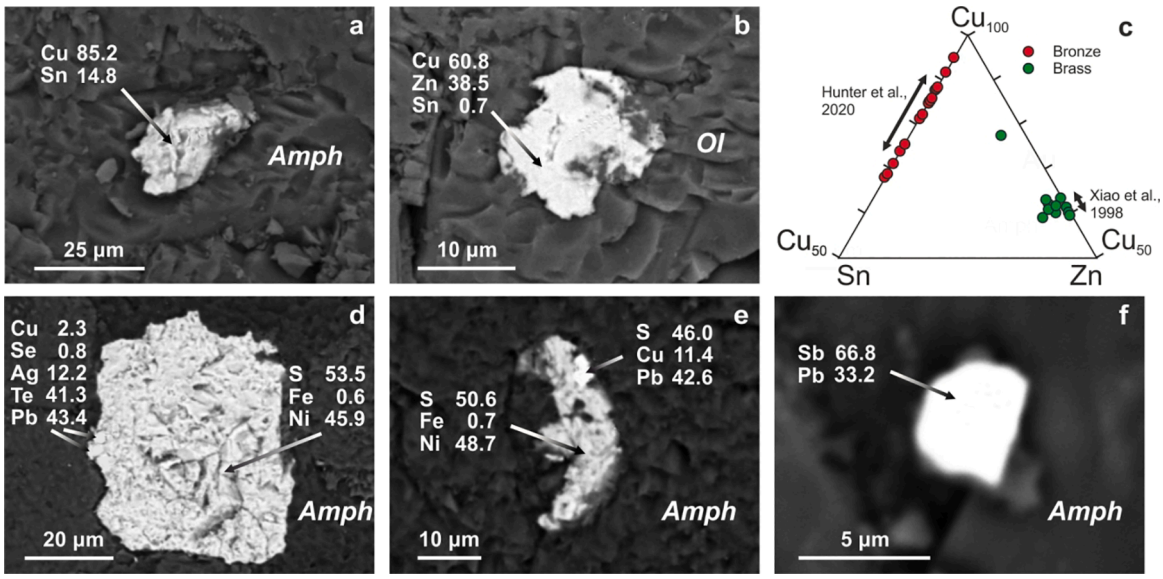

Fig. 7. SEM images of chalcophile metal compounds and associated minerals (a, b, d-f) and compositional variations in Cu-Sn-Zn compounds (c). a) tin-copper (natural bronze); b) tin-zinc-copper (natural brass); c) compositions of natural bronzes (Cu-Sn) and brasses (Cu-Zn) from the ILC compared with bronze alloys in vesicles from the Stromboli basalts (Hunter et al., 2020) and brasses (zinccopperite) from a copper-porphyry deposit in China (Xiao et al., 1998); d) inclusion of millerite (NiS) in Cu-Ag-bearing altaite (PbTe); e) inclusion of Cu-Pb sulfide in millerite (NiS); f) lead-antimony. Amph – amphibole, Ol – olivine.

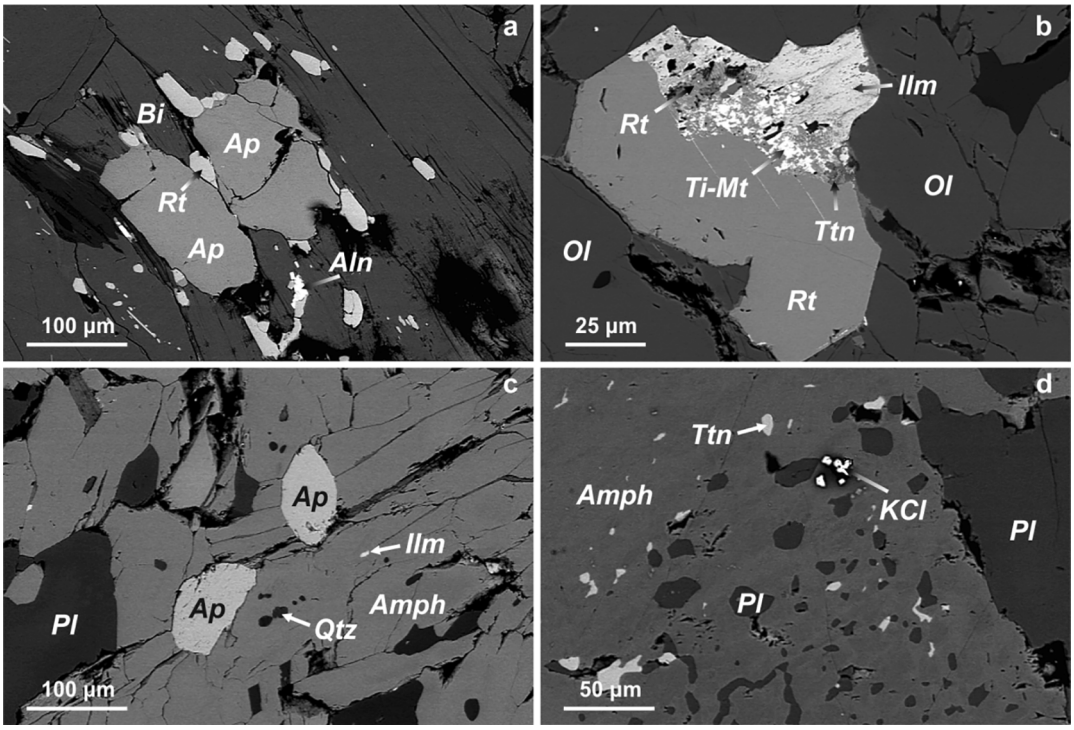

Fig. 8. SEM images of apatite (Ap), K-halide (KCl), titanite (Ttn), rutile (Rt), ilmenite (Ilm), Ti-magnetite (Ti-Mt), allanite (Aln) and quartz (Qtz) in ultramafic–mafic rocks from the ILC. a) apatite in association with rutile and allanite included in large biotite (Bi) oikocryst; b) large composite grain of rutile with transitional zone composed of fine-grained rutile, titanite and Ti-magnetite and thick (5–10 μm) rim formed by ilmenite surrounded by olivine (Ol); c) apatite, ilmenite and quartz included in large amphibole (Amph) in contact with plagioclase (Pl); d) small grains of plagioclase, K-halide and titanite included in amphibole (Amph) in contact with larger plagioclase grains.

the discrimination of arc rocks from oceanic (abyssal, plateau and ocean island) igneous assemblages (Condie, 2005). Magnesian K-lamprophyre dikes cross-cutting ultramafic-mafic rocks of the ILC exhibit elevated Rb and Nb and, especially TiO_2 and Ba contents (Fig. 3d) comparable to subduction-related alkaline magmas, such as absarokites, shoshonites and high-Nb basalts (Kepezhinskas et al., 1996, 2020; Liotard et al., 2008; Leslie et al., 2009). Biotite-hornblende dacite (Fig. 3d) is enriched in Al, Na, Sr and Ba and depleted in Y and Yb, which, together with high Sr/Y ratio of 320 classify it as typical adakite (Drummond et al., 1996; Defant and Kepezhinskas, 2001; Castillo, 2006). Adakites are widespread in the vicinity of the ILC, where they form numerous lava flows and isolated remnants of large caldera-type volcanic complexes (Buchko

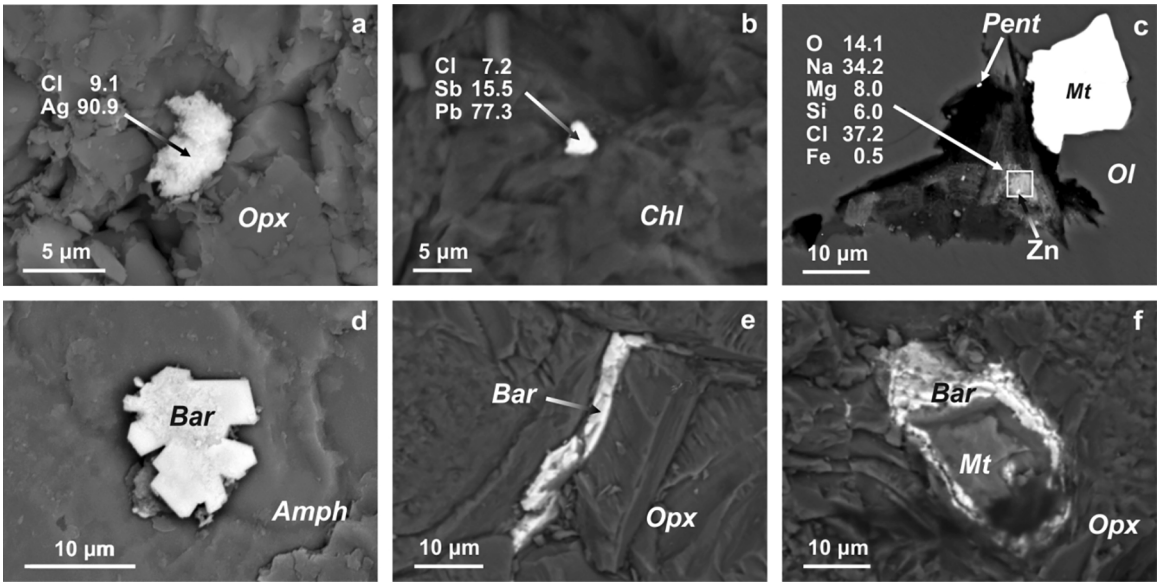

Fig. 9. SEM images of chlorine-bearing mineral phases and sulfates. A) silver with chlorine in orthopyroxene (Opx); b) antimony-lead with chlorine in chlorite (Chl); c) native zinc (Zn) and sodium chloride film mixed with olivine (Ol) within the decrepitated fluid inclusion (?); d) euhedral barite (Bar) in amphibole (Amph); e) folded lenticular barite (Bar) in orthopyroxene (Opx); f) barite (Bar) rim on magnetite (Mt) inclusion in orthopyroxene (Opx).

Table 4
Chemical composition of Cl-F apatites (wt. %).

Sample	IL-13	IL-13	IL-2	IL-2	IL-5	LU-1	LU-1	LU-1
O	38,7	39,1	39,4	39,9	37,7	37,8	38,5	38,8
Ca	36,5	36,5	37,8	37,8	35,4	38,4	38,9	38,6
Sr	N.d.	0.7	N.d.	N.d.	N.d.	N.d.	N.d.	N.d.
P	18,3	18,4	18,6	18,5	18,3	18,6	18,9	19,0
F	1,9	1,3	1,1	1,3	1,1	1,3	1,4	1,0
Cl	0,6	0,5	0,6	0,6	0,6	0,6	0,6	0,7
Total	96,0	96,5	97,5	98,1	93,1	96,7	98,3	98,1
F/Cl	3,2	2,6	1,8	2,2	1,8	2,2	2,3	1,4

N.d. – not detected

et al., 2016).

The ILC records prolonged (Late Triassic to Early Cretaceous – 233–114 Ma; Kepezhinskas et al., 2018, 2019) history of magmatism, metamorphism and metasomatism associated with Triassic subduction of the Mongol-Okhotsk ocean floor beneath the southern edge of the Siberian craton followed by Early Cretaceous collision and ocean closure (Fig. 11). Magmatic stage (Late Triassic) is marked by emplacement and crustal differentiation of arc-related basaltic or picritic magmas resulting in the formation of primary plutonic assemblages of Mg-olivine, Al-orthopyroxene, Cr-rich diopside, Fe-Mg-Al-Cr spinel, Al-rich pargasitic amphibole and

Ca-plagioclase. Pyroxenites in the ILC contain minor biotite, which may reflect either elevated alkalinity of parental melt, or potassic alteration related to the later-stage metasomatic processes. Many

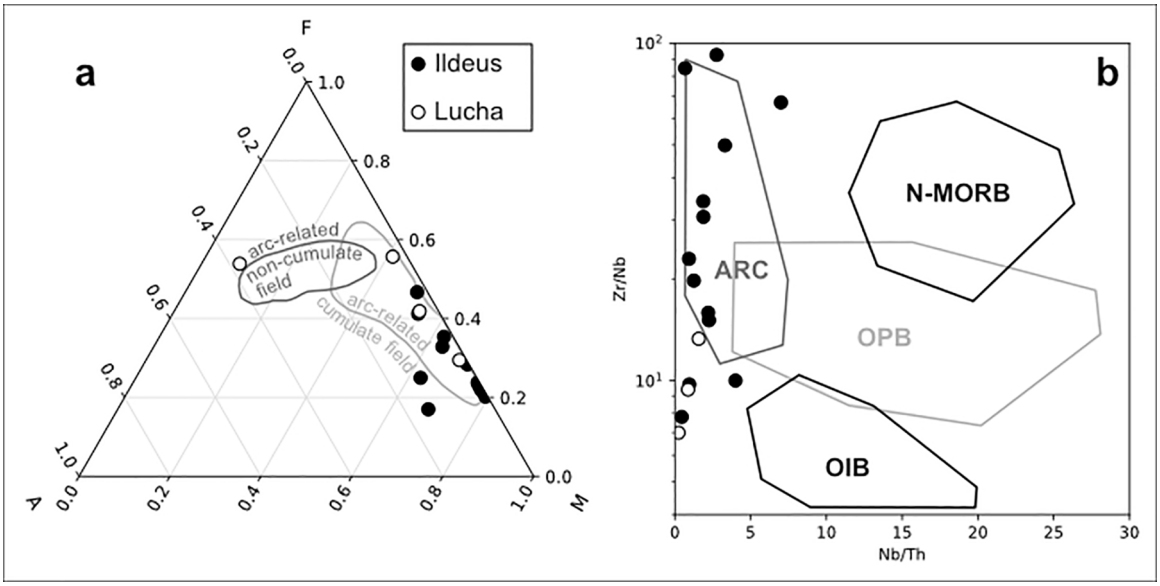

Fig. 10. Geochemistry of ultramafic–mafic rocks from the ILC reflecting their subduction-related tectonic setting. a) A (Na2O + K2O) - F (total FeO) - M (MgO) diagram with fields of arc-related cumulate and non-cumulate rocks from Beard (1986). b) Zr/Nb vs. Nb/Th. Fields for arc (ARC), depleted mid-ocean ridge basalts (N-MORB), ocean plateau basalts (OPB) and ocean island basalts (OIB) are from Condie (2005).

olivines in ultramafic-mafic rocks from the ILC are strongly depleted in Ca, Al, Ti and, in most cases, Cr (Table 1) in respect to typical magmatic olivines, which suggests metamorphic origin (Kamenetsky et al., 2016). Later-stage metamorphic (Early Cretaceous, ca.140 Ma) mineral assemblages include serpentine, tremolite, chlorite, Mg-hornblende, Cr-magnetite (serpentinization and greesnchist-facies metamorphism; Fig. 11) as well as Mn-rich, Ca-free olivine, Al-poor orthopyroxene and amphibole (amphibolite-facies metamorphism; Fig. 11). Finally, metasomatic paragenesis of mica, sericite, Cl-F-apatite, ilmenite, titanite, rutile, allanite and quartz is associated with Aptian (117–114 Ma) intrusions of adakite and potassic lamprophyre (Fig. 11).

6.2. *Magmatic versus metasomatic origin of metals and intermetallic compounds*

Ultramafic rocks of the ILC have undergone multiple episodes of serpentinization, metasomatism and metamorphism in conjunction with the Triassic subduction beneath the Siberian Craton followed by Cretaceous collision and closure of the Central Asian Ocean (Fig. 11; Kepezhinskas et al., 2019). Native metals and intermetallic compounds in the ILC occur in association with silicates, oxides, sulfates, sulfides and halides with both primary (magmatic) and secondary (metamorphic and metasomatic) textures as well as diverse chemical compositions indicative of their primary magmatic, metamorphic or metasomatic mode of origin.

Tungsten in the ILC occurs as sealed inclusions in Ni-rich olivine and Al-poor orthopyroxene with mesocumulate texture and in secondary textured amphibole. (Fig. 4a). Tungsten association with magmatic minerals and its high melting point suggests its formation under reduced conditions followed by magmatic transport to the crust by primitive basaltic melt. Native W, along with metallic Cr, Ni, Cu, Fe, Zn, Co, Cu-Ni, Pt-Fe-Ni-Cu, Fe-Cu-Ni, Ag-Au and Ag-Au-Fe alloys, W-Co-Fe-Ni-Si carbides, microdiamond, graphite and wüstite are present in chromitites from Luobusa (Tibet) and Ray-Iz (Polar Urals) supra-subduction zone ophiolites (Zhang et al., 2016). In addition, native metals such as Ni, Fe and possibly Ti along with Fe-silicides have been reported from mantle wedge xenoliths in the Kamchatka arc (Ishimaru et al., 2009). Native Si, Fe, Cu, Ni, Pt have been found along with Ti and Si carbides, Fe-Ni-Si and Fe-Cr alloys, diamond and graphite in subduction-related, carbonated xenoliths from the CAOB in northern China (Liu et al., 2015). These mineral assemblages have been interpreted as evidence for localized, highly reduced conditions in subduction-related lithosphere.

Native platinum (Fig. 4b) as well as FePt, Ni-Rh-Pt and Pd-Pt compounds (Fig. 5a, b, c) are included in magmatic olivine and orthopyroxene, occasionally replaced by chlorite (Fig. 5c), tremolite (Fig. 5c) and serpentine. Iron-platinum compounds occur in ultramafic-mafic igneous rocks (Barkov and Cabri, 2019) and subduction-related volcanics (Berdnikov et al., 2020). Native platinum was reported from mantle wedge peridotite xenoliths in Kamchatka and Patagonia (Kepezhinskas et al., 2002; Gonzalez-Jimenez et al., 2019). Presence of Ni (1.8 at.%; Fig. 5b) in rhodium-platinum compound is consistent with its magmatic origin (Genkin and Evstigneeva, 1986; Barkov and Cabri, 2019). However, since platinum is soluble in hydrothermal solutions over a range of pressures and temperatures (Gammons, 1996; Tagirov et al., 2019), the hydrothermal origin of platinum and Pt-bearing compounds in the ILC cannot be completely ruled out.

Native gold and silver along with a range of Cu-Ag, Zn-Cu-Ag, Zn-Cu-Au, Ag-Cu-Au and Ag-Ni-Zn-Cu-Au compounds occur in metamorphic or metasomatic Ca-poor, Mn-rich olivine (Fig. 6e), Al-poor, Fe-orthopyroxene (Fig. 5d, e and Fig. 6a, b), pargasitic amphibole (Fig. 6d), chlorite

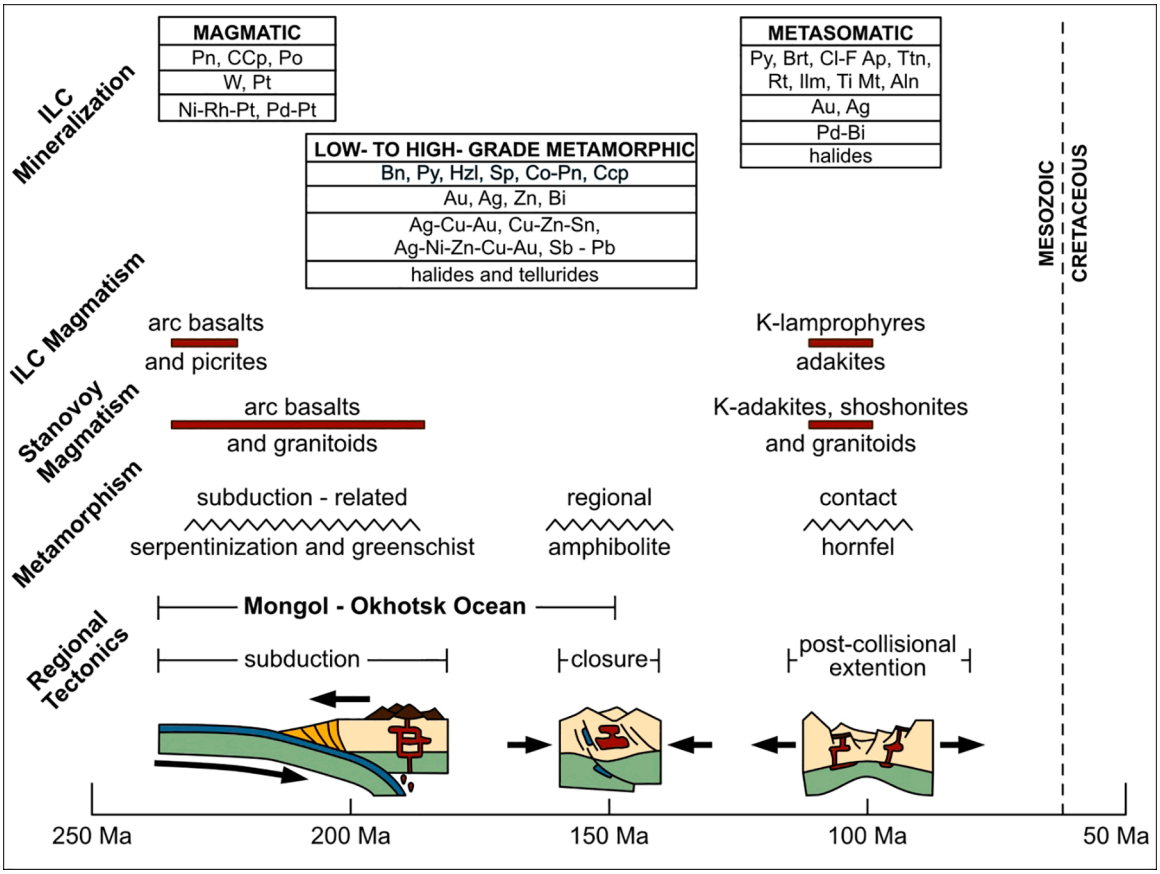

Fig. 11. Tectonic, magmatic and metamorphic events and metal-rich mineralization at the ILC. Additonal data used in this diagram are from Larin et al. (2006), Van der Voo et al. (2015) and Buchko et al. (2016). Mineral abbreviations: Pn - pentlandite, Co-Pn – Co-pentlandite, Po – pyrrhotite, Py – pyrite, Ccp – chalcopyrite, Sp – sphalerite, Bn – bornite, Dg – digenite, Hzl – heazlewoodite, Brt – barite, Ap – apatite, Ttn – titanite, Rt – rutile, Ilm – ilmenite, Ti-Mt – Ti-magnetite, Aln – allanite.

(Fig. 5f), biotite and tremolite (Table 3). Textures of intermetallic compounds and compositions of host silicates suggest a later-stage metasomatic origin for Cu-Ag-Au and Ag-Ni-Zn-Cu-Au compounds. Most probably Au and Ag were introduced by hydrothermal fluids, while Cu, Ni and Zn, at least partially, were leached from magmatic and metasomatic sulfides (e.g., pentlandite, chalcopyrite, bornite and sphalerite; Table 3). Presence of digenite is consistent with elevated copper mobility during hydrothermal alteration of ultramafic–mafic rocks in the ILC. Sluzhenikin and Mokhov (2014) documented late-stage deposition of Au, Ag, Sn, Sb, Pb and Cu-Au-Ag alloys by chlorine-rich hydrothermal fluids in Noril'sk primary sulfide ore. We propose a similar mode of formation for Cu-Ag (Fig. 5d, e, f), Ag-Cu-Au (Fig. 6a, b), Ag-Ni-Zn-Cu-Au (Fig. 6d), Zn-Cu-Ag (6e), Zn-Cu-Au (Fig. 6f) and Pb-Sb (Fig. 9b) compounds, as well as native gold (Fig. 4c), silver (Fig. 4d), zinc (Fig. 4e and Fig. 9c) and bismuth (Fig. 4f) in the ILC. Zinc-copper alloys in the ILC are chemically similar (Fig. 7c) to natural brasses (zinccopperites) reported from some copper porphyry deposits in China (Xiao et al., 1998). Notably, Au, Ag, Zn, Pb, Sn and Sb could have been introduced by hydrothermal (350–500 °C) fluids (Sluzhenikin and Mokhov, 2014), while Ni and Cu were, at least partially, scavenged from primary magmatic sulfides such as pentlandite, bornite and chalcopyrite. Fluid-induced deposition has been proposed for Sn-Cu (with, or without cobalt) alloys in Stromboli basalts (Hunter et al., 2020), as well as Sn-Cu (natural bronze) and Zn-Cu (natural brass, or zinccopperite) compounds in epithermal gold and copper porphyry deposits in southwestern China (Xiao et al., 1998; Xie et al., 2006; Liu et al., 2008). Alternatively, Ag-Cu-Au compounds, as relatively high-temperature phases (>1000 °C; Chudnenko and Pal'yanova, 2014), may represent relic magmatic assemblages, partially recrystallized during the later-stage metasomatic imprint by subduction-related fluids.

6.3. Effects of serpentinization

Native metals and intermetallic compounds in the ILC are frequently found in variably serpentinized ultramafic rocks (Table 3). Other secondary minerals associated with metals, besides serpentine, include chlorite, tremolite, amphibole, biotite, sericite, Cr-magnetite, as well as secondary sulfides (digenite and heazlewoodite). However, serpentine (frequently with detectable Cl) remains a dominant silicate phase in these hydrothermally altered ultramafic lithologies.

Serpentinization of orthopyroxene-bearing, olivine-rich ultramafic rocks may cause their enrichment in various metal-rich phases, such as Fe-Ni-Cu sulfides, alloys and native metals (Donaldson, 1981; Rossetti and Zucchetti, 1988). In the course of serpentinization, olivine reacts with water to form serpentine, magnetite and hydrogen due to oxidation of Fe^{2+} to Fe^{3+} (Frost, 1985), which together with low fluid/rock ratio during serpentinization results in progressive reduction of oxygen and sulfur (Klein and Bach, 2009). In addition, methane can be produced in serpentinization reactions in the case of significant carbon presence (Frost, 1985; Frost and Beard, 2007; Früh-Green et al., 2004; McCollom, 2016). Consequently, very low redox conditions (approaching the iron-magnetite buffer) can be associated with serpentinization, as suggested by experimental data (Berndt et al., 1996), thermodynamic modeling (Frost, 1985; Evans, 2008) and frequent occurrence of metallic phases such as S-poor sulfides (e.g., heazlewoodite), native copper, and Fe-Ni alloys in serpentinized peridotites (Dick, 1974; Marchesi et al., 2013; Schwarzenbach et al., 2014). Field and fluid inclusions studies indicate that reducing conditions may also persist through the deserpentinization and regional prograde metamorphism of large peridotite bodies in Alpine-type orogenic belts (Peretti et al., 1992; Brovarone et al., 2017). In addition, formation of awaruite (along with pentlandite, heazlewoodite and magnetite) in ultramafic rocks has been ascribed to progressive serpentinization (Sciortino et al., 2015).

Native metals and intermetallic compounds associated with metamorphic and metasomatic phases in the ILC (amphibole, Ca-poor, Mn-rich olivine, Al-poor pyroxenes, biotite, chlorite and serpentine) often contain minor amounts of Ni, Cu and Co, possibly reflecting remobilization of primary Ni-Cu-Co-Fe sulfides (such as pentlandite, Co-pentlandite and chalcopyrite). High concentrations of hydrogen and methane realized during serpentinization may assist reduction of these sulfides to native metals (Cu) and alloys (Ni-Fe), while later-stage metasomatic overprints, which introduced fluid-mobile siderophile (Au) and chalcophile (Ag, Zn, Sn, Pb, Sb) metals result in the formation of compositionally heterogeneous Ni-Cu-Ag-Au and Cu-Sn-Pb-Sb compounds. Native platinum (Fig. 4b) and, possibly, Pt compounds (with Fe, Ni, Rh and Pd) could have also formed during serpentinization of the ILC rocks, as free Pt was produced in association with Fe-Ni alloys during low-temperature (200–320 °C) olivine serpentinization experiments in presence of CO_2 (McCollom, 2016).

6.4. Role of halogen-rich fluids

Native metals and metal alloys in the ILC are frequently associated with halogen-rich mineral phases, such as metal halides (Table 3; Fig. 5e, 8d, 9a, b, c). Sodium and potassium halides occur as thin films in decrepitated fluid inclusions in olivine (Fig. 9c) or aggregates of microparticles in metasomatic orthopyroxene and amphibole (Fig. 5e and Fig. 8d). Chlorine-rich silver (Fig. 10a) and Cl-rich antimony-lead compound (Fig. 9b) occur in orthopyroxene and chlorite, respectively. Halogens were detected in pargasitic amphibole (0.1–2.7 wt% Cl, 0.8 wt % Br), biotite (0.11–0.13 wt% Cl), chlorite (0.07–0.22 wt% Cl) and serpentine (0.11 wt% Cl) (Kepezhinskas et al., 2019). F/Cl ratios in apatites from metal-bearing pyroxenites and gabbros (Table 4) are broadly similar to arc and back-arc basin basalts and supra-subduction peridotites (0.04–2; Barnes et al., 2018) and have distinctly lower F/Cl ratios than subduction-related metamorphic fluids (114–413 in metamorphic apatites and 10–100 in calculated fluid phase; Page et al., 2016). Distribution of halogens in arc lavas (Dalou et al., 2014 and references therein) suggests that arcs can be roughly grouped into "high-Cl" (F/Cl ratios < 1) and "low-Cl" (F/Cl ratios < 1) types (e.g., Fig. 5 in Dalou et al., 2014). Since seawater is nearly 15,000 times richer in Cl than F (Cl_{ave} = 19,350 ppm, F_{ave} = 1.3 ppm; Kendrick, 2018) and chlorine is highly soluble in slab-derived hydrous fluids (Brennan, 1993), the majority of melt inclusions and glasses in volcanic arcs have F/Cl ratios of 0.8 and lower (Dalou et al., 2014). This is consistent with estimated F/Cl ratio in slab-derived aqueous fluid of about 0.1–0.25 (Dalou et al., 2014). In contrast, some arcs (Kermadec, Kamchatka, Central America, Cascades) display F/Cl ratios in excess of 1, similar to the slab melt component (F/Cl ratio of ~1) reported from Mount Shasta basalts (Le Voyer et al., 2010). This appears to suggest that apatites in the ULC rocks crystallized in response to the intrusion of Early Cretaceous adakites (e.g. amphibole-mica dacites with Sr/Y = 320; Table 2; Fig. 3e) and reflect, to a certain extent, halogen signature of H_2O-rich slab melts rather than aqueous fluids. Adakite dikes and veins impregnate ultramafic rocks (Kepezhinskas et al., 2019), while adakite lavas and tuffs form large volcanic paleo-calderas in the immediate vicinity of the ILC (Buchko et al., 2016).

Co-occurrence of halides with platinum- and gold-based intermetallic compounds in the ILC suggests presence of halogen-rich fluids either during their magmatic crystallization or, alternatively, during later-stage metasomatism. Experimental data (Gammons, 1996; Tagirov et al., 2019) and evidence from ultramafic-mafic intrusions (Boudreau et al., 1986) suggest that PGM are soluble in chlorine-rich aqueous fluids within the wide range of temperatures (100–600 °C). Additionally, theoretical considerations and thermodynamic modeling emphasize that significant solubility of platinum (>10 ppb) in aqueous fluids (25–300 °C) can be achieved only under highly oxidizing and acidic conditions (Gammons, 1996). Platinum mineralization of undeniable hydrothermal origin occurs in the Bushveld complex (Waterberg deposit; Oberthür et al., 2018), Duluth (Babbitt deposit; Mogessie et al., 1991) and Salt Chuck (Watkinson and Melling, 1992) layered intrusions. Another set of data suggests that platinum and gold have low solubility

in hydrothermal fluids with or without chlorine, especially in presence of elevated Ni concentrations at 300–500 °C and 1 kbar (Likhoidov et al., 2008) and 400–500 °C and 800 bar (Scholten et al., 2018). Scholten et al. (2018) have specifically stressed that "platinum remains practically immobile in such [chloridic] fluids at any HCl concentration that is conceivable to occur in nature". It was also demonstrated, using sulfide-komatiite assemblages, that platinum can be transported as bisulfide complexes in near-neutral solutions under reduced oxidation conditions, but that it remains rather immobile even in most altered ultramafic-mafic silicate rocks (Barnes and Liu, 2012). Parkinson et al. (1992) reported low concentrations of platinum (as well as palladium) in serpentinites from the Mariana forearc indicating low mobility of these highly siderophile elements during low-temperature hydrothermal alteration of supra-subduction zone peridotites. These authors also did not detect any Pt or Pd in fluids expelled from serpentinite muds within the Conical Seamount in Mariana forearc (Parkinson et al., 1992). On the other hand, platinum solubility in silicate melts and high-temperature magmatic fluids under the range of P-T conditions is well documented (Bennett et al., 2014). High-temperature (1250 °C) experiments demonstrate that abundance of platinum micro-nuggets increases with Cl content in the system offering "compelling evidence that Cl-bearing fluids have the capacity to transport significant amount of Pt and Ir under magmatic conditions " (Blaine, 2010). Blaine (2010) suggested that estimated Pt concentrations in the Cl-bearing fluid are on the order of a few hundred parts per million as opposed to ppb levels for platinum contents in co-exisiting silicate melts, which is consistent with presence of magmatic halide inclusions in the Ultramafic and Lower Banded Series of the Stillwater Complex in Montana (Hanley et al., 2008). Based on the above, at least some of the platinum-rich compounds in the ILC could have formed under magmatic conditions in presence of high-temperature Cl-bearing fluids.

Other ore metals such as gold, silver, copper, zinc, tin, lead and antimony are highly soluble in chlorine-rich, aqueous fluids (Gammons and Williams-Jones, 1995; Wilkinson et al., 2019; Scholten et al., 2018). During percolation through crustal magmatic conduits, metal-bearing fluids are affected by several processes that trigger deposition of ore metals including decompression, boiling, cooling, fluid-rock interaction and mixing with meteoric waters (Pokrovsky et al., 2013). Fractionation of these fluids during vapor-brine and fluid-rock interactions will cause most ore metals to partition into the saline fluid phase (Pokrovsky et al., 2013; Audetat, 2019). As metals can be present as different species in hydrothermal solutions, changes in fluid chemistry due to assimilation of external carbonaceous matter or release of abiogenic reducing gases (hydrogen, methane, other hydrocarbons), may facilitate deposition of metals in crustal conduits (Hanley et al., 2005; Suintilan et al., 2019). This might be especially true in case of a long-lived crustal plumbing system, such as the ILC, where assimilation of carbon-rich host rocks was documented both geologically and on the basis of sulfur isotope signatures of hydrothermal sulfides (Buchko et al., 2002; Kepezhinskas et al., 2019).

6.5. Redox heterogeneity in subduction zones

Subduction zones are generally considered to be highly oxidized environments (Ballhaus, 1993; Parkinson and Arculus, 1999; Evans et al., 2012; Iacovino et al., 2020). However, recent studies indicate existence of reduced mantle wedge prior to the onset of subduction and subsequent slab devolatilization (Evans, 2012; Nebel et al., 2015). Birner et al. (2017) suggested that "forearc mantle is not pervasively oxidized relative to mid-ocean ridge, and that the asthenospheric mantle in the proto-subduction zone region is not oxidized prior to subduction initiation". In general, addition of slab-derived hydrous fluid to the mantle wedge causes oxidation and flux-induced melting producing uniformly oxidized, hydrous primitive magmas in volcanic arcs (Kelley and Cottrell, 2009). However, Piccoli et al. (2019) demonstrated that subducting oceanic lithosphere (serpentinites) is capable of releasing a reduced, rather than an oxidized, fluid component into the overlying mantle wedge. Petrologic observations suggest that carbonate reduction in subduction zones releases large volumes of abiotic hydrocarbons (Tao et al., 2018) and that reducing gases such as hydrogen and methane can be a common component of slab fluid, largely responsible for the geochemical signature of arc magmas (Brovarone et al., 2017). This is consistent with the occurrence of hydrocarbon (methane and other aliphatic and cyclic hydrocarbons)-rich fluid inclusions in subduction-related harzburgite xenoliths from China (Song et al., 2009) and Kamchatka (Sharapov et al., 2017). Ishimaru et al (2009) proposed that native nickel, iron and Fe-silicides, spatially associated with fluid inclusions in Kamchatka xenoliths, were formed in the presence of reducing fluids during serpentinization of peridotite along the crust-mantle interface in the Kamchatka subduction zone and that this localized redox phenomenon might be present in other volcanic arcs. Occurrence of native metals and intermetallic compounds in the ILC is consistent with the localized reduced conditions in otherwise oxidized crust of the Mesozoic Stanovoy magmatic arc. Close textural relationships between metals, alteration and chlorine-bearing phases suggest that reduced fluids were either produced *in-situ* during serpentinization and/or metasomatism of ultramafic rocks at mid-crustal levels or were introduced via carbonate reduction from the underlying slab.

7. Conclusions

(1) Ultramafic-mafic rocks of the Ildeus-Lucha Complex (ILC) were emplaced in Late Triassic (232–233 Ma) within the Stanovoy convergent margin and subjected to hydrothermal alteration and metamorphism at ~140 Ma related to the closure of Mongol-Okhotsk oceanic basin. New geochemical data presented in this paper suggest that ultramafic rocks are intruded by Early Cretaceous (114–117 Ma) adakites and shoshonitic lamprophyres. All ILC rocks display prominent depletions in high-field strength elements and were formed through differentiation of arc mafic melts in crustal magmatic conduits.

(2) Dunites, wehrlites and pyroxenites from the ILC carry an unusual suite of native metals (W, Pt, Au, Ag, Zn, Bi) and intermetallic compounds (Cu-Au-Ag, Cu-Ag, Pt-Pd, Ni-Rh-Pt, Fe-Pt, Cu-Zn-Sn, Pb-Sb), which are frequently associated with halides and F-Cl-apatites. In addition, ultramafic rocks contain primary (pentlandite, Co-pentlandite, millerite, chalcopyrite, bornite) and secondary (heazlewoodite, digenite, pyrite, sphalerite) sulfides.

(3) Textural and compositional data on metal assemblages presented in this paper indicate a) crystallization (W and, possibly, Pt) from metal-rich arc magmas under unusually reduced conditions in subduction-related lithosphere; b) formation from magmatic sulfides during pervasive serpentinization and release of abiogenic hydrogen and hydrocarbons and c) precipitation from chlorine-rich, fractionated saline fluids possibly associated with collision-related metasomatism of the Stanovoy island arc crust.

(4) These localized reduced conditions in the Stanovoy subduction zone could have been a) inherited from redox-heterogeneous subduction-related lithosphere prior to oxidizing slab flux or b) related to large-scale liberation of hydrogen and methane during serpentinization or carbonate reduction in the arc crust.

Declaration of Competing Interest

The authors declare that they have no known competing financial interests or personal relationships that could have appeared to influence the work reported in this paper.

Acknowledgments

Reviews from two anonymous referees significantly improved this paper. We thank Prof. Vadim (Dima) Kamenetsky and Dr. Maya

Kamenetsky for their hospitality, advice and help during N.P.K. stay at the University of Tasmania, Hobarth, Tasmania, Australia. Discussions with Prof. Ambre Luguet, Prof. Elisabeth Widom and Dr. David Kuentz in regards to the oxidation state of subduction zones were very helpful and illuminating. Mr. Tore Birkeland and Khingan Minerals AS are thanked for their continuous enthusiasm and support of our field and analytical endeavors.

Appendix A. Supplementary data

Supplementary data to this article can be found online at https://doi.org/10.1016/j.oregeorev.2020.103800.

References

Audetat, A., 2019. The metal content of magmatic-hydrothermal fluids and its relationship to mineralization potential. Econ. Geol. 114, 1033–1056.
Ballhaus, C., 1993. Redox state of lithospheric and asthenospheric upper mantle. Contrib. Miner. Petrol. 114, 331–348.
Barkov, A.Y., Cabri, L.J., 2019. Variations of major and minor elements in Pt-Fe alloy minerals: a review and new observations. Minerals 9 (25). https://doi.org/10.3390/min9010025.
Barnes, S.J., Liu, W., 2012. Pt and Pd mobility in hydrothermal fluids: evidence from komatiites and from thermodynamic modeling. Ore Geol. Rev. 44, 49–58.
Barnes, J.D., Manning, C.E., Scambelluri, M., Selverstone, J., 2018. The behavior of halogens during subduction-zone processes. In: Harlov, D.E., Aranovich, L. (Eds.), The Role of Halogens in Terrestrial and Extraterrestrial Geochemical Processes. Springer Geochemistry.
Beard, J.S., 1986. Characteristic mineralogy of arc-related cumulate gabbros: implications for the tectonic setting of gabbroic plutons and for andesite genesis. Geology 14, 848–851.
Bennett, N.R., Brenan, J.M., Koga, K.T., 2014. The solubility of platinum in silicate melt under reducing conditions: results from experiments without metal inclusions. Geochemica et Cosmochimica Acta 133, 422–442.
Berdnikov, N.V., Nevstruev, V.G., Kepezhinskas, P.K., Mochalov, A.G., Yakubovich, O.V., 2020. PGE mineralization in andesite breccias associated with the Poperechny iron-manganese deposit (Lesser Khingan, Far East Russia): whole-rock geochemical, ^{190}Pt-^{4}He isotopic, and mineralogical evidence. Ore Geol. Rev. 118, 103352.
Berndt, M.E., Allen, D.E., Seyfried, W.E., 1996. Reduction of CO_2 during serpentinization of olivine at 300°C and 500 bar. Geology 24, 351–354.
Birner, S.K., Warren, J.M., Cottrell, E., Davis, F.A., Kelley, K.A., 2017. Forearc peridotites from Tonga record heterogeneous oxidation of the mantle following subduction initiation. J. Petrol. 58, 1755–1780.
Blaine, F.A., 2010. The effect of volatiles (H_2O, Cl and CO_2) on the solubility and partitioning of platinum and iridium in fluid-melt systems. Ph.D. Dissertation. University of Waterloo, Canada, p. 170 p..
Boudreau, A.E., Mathez, E.A., McCallum, I.S., 1986. Halogen geochemistry of the Stillwater and Bushveld Complexes: evidence for transport of the platinum-group elements by Cl-rich fluids. J. Petrol. 27, 967–986.
Brandon, A.D., Draper, D.S., 1996. Constraints on the origin of the oxidation state of mantle overlying subduction zones: an example from Simcoe, Washington, USA. Geochim. Cosmochim. Acta 60, 1739–1749.
Brennan, J., 1993. Partitioning of fluorine and chlorine between apatite and aqueous fluids at high pressure and temperature: implications for the F and Cl content of high P-T fluids. Earth Planet. Sci. Lett. 117, 251–263.
Brounce, M.N., Kelley, K.A., Cottrell, E., 2014. Variations in $Fe^{3+}/\Sigma Fe$ of Mariana arc basalts and mantle wedge fO_2. J. Petrol. 55, 2513–2536.
Brovarone, A.V., Martinez, I., Elmaleh, A., Compagnoni, R., Chaduteau, G., Ferraris, C., Esteve, I., 2017. Massive production of abiotic methane during subduction evidenced in metamorphosed ophicarbonates from the Italian Alps. Nature Commun. 8 (14134) https://doi.org/10.1038/ncomms/14134.
Buchko, I.V., Izokh, A.E., Nosyrev, M.Y., 2002. Sulfide mineralization in ultrabasic-basic rocks from the Stanovoy megablock. Pac. Geol. 21, 56–68.
Buchko, I.V., Sorokin, A.A., Ponomarchuk, V.A., Kotov, A.B., Travin, A.V., Kovach, V.P., 2016. Trachyandesites of the Mogot volcanic field (Stanovoi volcanoplutonic belt, East Siberia): age, geochemical features, and sources. Russ. Geol. Geophys. 57, 1389–1397.
Bucholz, C.E., Kelemen, P.B., 2019. Oxygen fugacity at the base of the Talkeetna arc, Alaska. Contr. Mineral. Petrol. 174, 79.
Castillo, P.R., 2006. An overview of adakite petrogenesis. Chin. Sci. Bull. 51, 257–268.
Chamberlain, J.A., McLeod, C.R., Traill, R.J., Lachance, C.R., 1965. Native metals in the Muscox intrusion. Can. J. Earth Sci. 2, 188–215.
Chudnenko, K.V., Pal'yanova, G.A., 2014. Thermodynamic properties of solid solutions in the Ag-Au-Cu system. Russ. Geol. Geophys. 55, 349–360.
Condie, K.C., 2005. High field strength element ratios in Archean basalts: a window to evolving sources of mantle plumes? Lithos 79, 491–504.
Dalou, C., Koga, K.T., Le Voyer, M., Shimizu, N., 2014. Contrasting partition behavior of F and Cl during hydrous melting: implications for Cl/F signature in arc magmas. Progress in Earth and Planetary. Science 1 (26). https://doi.org/10.1186/s40645-014-0026-1.
DeBari, S.M., Coleman, R.G., 1989. Examination of the deep levels of an island arc: evidence from the Tonsina ultramafic-mafic assemblage, Tonsina, Alaska. J. Geophys. Res. 94, 4373–4391.
Defant, M.J., Kepezhinskas, P., 2001. Evidence suggests slab melting in arc magmas. EOS Trans. Am. Geophys. Union 82, 65–69.
Dick, H.J.B., 1974. Terrestrial nickel-iron from the Josephine Peridotite, its geologic occurrence, associations, and origin. Earth Planet. Sci. Lett. 24, 291–298.
Didenko, A.N., Kaplun, V.B., Malyshev, Yu.F., Shevchenko, B.F., 2010. Lithospheric structure and Mesozoic geodynamics of the eastern Central Asian fold belt. Russ. Geol. Geophys. 51, 492–506.
Donaldson, M.J., 1981. Redistribution of ore elements during serpentinization and talc-carbonate alteration of some Archean dunites, Western Australia. Econ. Geol. 76, 1698–1713.
Drummond, M.S., Defant, M.J., Kepezhinskas, P.K., 1996. Petrogenesis of slab-derived trondhjemite-tonalite-dacite/adakite magmas. Trans. R. Soc. Edinburgh: Earth Sci. 87, 205–215.
Elliott, T.R., Plank, T., Zindler, A., White, W.M., Bourdon, B., 1997. Element transport from slab to volcanic front in the Mariana arc. J. Geophys. Res. 201, 14991–15019.
Evans, B.W., 2008. Control of the products of serpentinization by the $Fe^{2+}Mg_{-1}$ exchange potential of olivine and orthopyroxene. J. Petrol. 49, 1873–1887.
Evans, K., Elburg, M.A., Kamenetsky, V.S., 2012. The oxidation state of sub-arc mantle. Geology 40, 783–786.
Frost, B.R., 1985. On the stability of sulfides, oxides, and native metals in serpentinite. J. Petrol. 26, 31–63.
Frost, B.R., Beard, J.S., 2007. On silica activity and serpentinization. J. Petrol. 49, 1351–1368.
Früh-Green, G.L., Connnoly, J.A.D., Plas, A., Kelley, D.S., Grobety, B., 2004. Serpentinization of oceanic peridotites: implications for geochemical cycles and biological activity. In: The Subseafloor Biosphere at Mid-Ocean Ridges. Geophysical Monograph Series 144, 119–136.
Gammons, C.H., 1996. Experimental investigations of the hydrothermal geochemistry of platinum and palladium. V. Equilibria between platinum, Pt (II) and Pt (IV) chloride complexes at 25 to 300°C. Geochim. Cosmochim. Acta 60, 1683–11614.
Gammons, C.H., Williams-Jones, A.E., 1995. The solubility of Au-Ag alloy+AgCl in HCl/NaCl solutions at 300°C: new data on the stability of Au(I) chloride complexes in hydrothermal fluids. Geochim. Cosmochim. Acta 59, 3453–3468.
Genkin, A.D., Evstigneeva, T.L., 1986. Association of platinum-group minerals of the Noril'sk copper-nickel sulfide ores. Econ. Geol. 81, 1203–1212.
Gonzalez-Jimenez, J.M., Roque-Posell, J., Jimenez-Franco, A., Tassara, S., Nieto, F., Gervilla, F., Baurier, S., Proenza, J.A., Saunders, E., Deditius, A.P., Schilling, M., Corgne, A., 2019. Magmatic platinum nanoparticles in metasomatic silicate glasses and sulfides from Patagonian mantle xenoliths. Contrib. Miner. Petrol. 147 (47) https://doi.org/10.1007/200410-019-1583-5.
Grossley, R.J., Evans, K.A., Evans, N.J., Bragagni, A., McDonald, B.J., Reddy, S.M., Speelmanns, I., 2020. Tracing highly siderophile elements through subduction: insights from high-pressure serpentinites and "hybrid" rocks from Alpine Corsica. J. Petrol. https://doi.org/10.1093/petrology/egaa030.
Grove, T.L., Chatterjee, N., Parman, S.W., Medard, E., 2006. The influence of H_2O on mantle wedge melting. Nature 459, 694–697.
Grove, T.L., Till, C.B., Krawczynski, M.J., 2012. The role of H_2O in subduction zone magmatism. Ann. Rev. Earth Planetary Sci. 40, 413–439.
Hanley, J.J., Mungall, J.E., Pettke, T., Spooner, E.T.C., Bray, C.J., 2005. Ore metal redistribution by hydrocarbon-brine and hydrocarbon-halide melt phases, North Range footwall of the Sudbury Igneous Complex, Ontario, Canada. Miner. Deposita 40, 237–256.
Hanley, J.J., Mungall, J.E., Pettke, T., Spooner, E.T.C., Bray, C.J., 2008. Fluid and halide melt inclusions of magmatic origin in the Ultramafic and Lower Banded Series, Stillwater Complex, Montana, USA. J. Petrol. 49, 1133–1160.
Hochstaedter, A., Gill, J., Peters, R., Broughton, P., Holden, P., 2001. Across-arc geochemical trends in the Izu-Bonin arc: contributions from the subducting slab. Geochem. Geophys. Geosyst. 2.
Hunter, E.A.O., Hunter, J., Zajacz, Z., Keith, J.D., Hann, N.L., Christiansen, E.H., Dorais, M.J., 2020. Vapor transport and deposition of Cu-Sn-Co-Ag alloys in vesicles in mafic volcanic rocks. Econ. Geol. 115, 279–301.
Iacovino, K., Guild, M.R., Till, C.B., 2020. Aqueous fluids are effective oxidizing agents of the mantle in subduction zones. Contrib. Miner. Petrol. 175 https://doi.org/10.1007/s00410-020-1673-4.
Ionov, D.A., 2010. Petrology of mantle wedge lithosphere: new data on supra-subduction zone peridotite xenoliths from the andesitic Avacha volcano, Kamchatka. J. Petrol. 51, 327–361.
Ishimaru, S., Arai, S., Shukuno, H., 2009. Metal-saturated peridotite in the mantle wedge inferred from metal-bearing peridotite xenoliths from Avacha volcano, Kamchatka. Earth Planet. Sci. Lett. 284, 352–360.
Jahn, B.M., 2004. The Central Asian Orogenic Belt and growth of the continental crust in the Phanerozoic. In: Malpas, J., Fletcher, C.J.N., Ali, J.R., Aitchison, J.C. (eds). Aspects of the tectonic evolution of China. Geological Society, London, Special Publication 226, 73-100.
Jahn, B.M., Wu, F., Chen, B., 2000. Granitoids of the Central Asian Orogenic Belt and continental growth in the Phanerozoic. Trans. R. Soc. Edinburgh: Earth Sci. 91, 181–193.
Jenner, F.E., O'Neill, H., St, C., Arculus, R.J., Mavrogenes, J.R., 2010. The magnetite crisis in the evolution of arc-related magmas and the initial concentration of Au, Ag and Cu. J. Petrol. 51, 2445–2464.
Kamenetsky, V.S., Lygin, A.V., Foster, J.G., Meffre, S., Maas, R., Kamenetsky, M.B., Goemann, K., Beresford, S.W., 2016. A story of olivine from McIvor Hill complex

(Tasmania, Australia): clues to the origin of the Avebury metasomatic Ni sulfide deposit. Am. Mineral. 101, 1321–1331.
Kelley, K.A., Cottrell, E., 2009. Water and the oxidation state of subduction zone magmas. Science 325, 605–607.
Kendrick, M.A., 2018. Halogens in seawater, marine sediments and the altered oceanic lithosphere. In: Harlov, D.E., Aranovich, L. (Eds.), The Role of Halogens in Terrestrial and Extraterrestrial Processes. Springer Geochemistry, pp. 591–648.
Kent, A.J.R., Elliott, T.R., 2002. Melt inclusions from Marianas arc lavas: implications for the composition and formation of island arc magmas. Chem. Geol. 183, 263–286.
Kepezhinskas, K.B., 1986. Structural-metamorphic evolution of Late Proterozoic ophiolites and Precambrian basement in the Central Asian Foldbelt of Mongolia. Precambr. Res. 33, 209–223.
Kepezhinskas, P., Defant, M.J., 2001. Non-chondritic Pt/Pd ratios in arc mantle xenoliths: evidence for platinum enrichment in depleted island-arc mantle sources. Geology 29, 851–854.
Kepezhinskas, P.K., Kepezhinskas, K.B., Pukhtel, I.S., 1991. Lower Paleozoic oceanic crust in Mongolian Caledonides: Sm-Nd isotope and trace element data. Geophys. Res. Lett. 18, 1301–1304.
Kepezhinskas, P.K., Reuber, I., Tanaka, H., Miyashita, S., 1993. Zoned calc-alkaline plutons in Northeastern Kamchatka, Russia: implications for the crustal growth in magmatic arcs. Mineral. Petrol. 49, 147–174.
Kepezhinskas, P.K., Defant, M.J., Drummond, M.S., 1996. Progressive enrichment of island arc mantle by melt-peridotite interaction inferred from Kamchatka xenoliths. Geochim. Cosmochim. Acta 60, 1217–1229.
Kepezhinskas, P.K., Defant, M.J., Widom, E., 2002. Abundance and distribution of PGE and Au in the island-arc mantle. Lithos 60, 113–128.
Kepezhinskas, P.K., Kepezhinskas, N.P., Kamenetsky, V.S., Berdnikov N.V., 2018. Multi-stage magmatic to metamorphic formation of Ni-Co-Cu-PGE-Au mineralization in a subduction-related setting: a case study of the Ildeus-Lucha complex (Stanovoy Mobile Belt, SE Siberia). Abstracts of the 2018 GSA Annual Meeting, Indianapolis, USA.
Kepezhinskas, P., Kepezhinskas, N., Berdnikov, N., 2019. Gold, platinum and palladium enrichments in arcs: role of mantle wedge, arc crust and halogen-rich slab fluids. E3S Web of Conferences 98, 08010. https://doi.org/10.1051/e3conf/20199808010.
Kepezhinskas, N., Kamenov, G.D., Foster, D.A., Kepezhinskas, P., 2020. Petrology and geochemistry of alkaline basalts and gabbroic xenoliths from Utila Island (Bay Islands, Honduras): insights into back-arc processes in the Central American volcanic arc. Lithos 352–353. https://doi.org/10.1016/j.lithos.2019.105306.
Keppler, H., 2017. Fluids and trace element transport in subduction zones. Am. Mineral. 102, 5–20.
Kerrich, R., Xie, Q., 2002. Compositional recycling structure of an Archean super-plume: Nb-Th-U-LREE systematics of Archean komatiites and basalts revisited. Contrib. Miner. Petrol. 142, 476–484.
Klein, F., Bach, W., 2009. Fe-Ni-Co-O-S phase relations in peridotite-seawater interactions. J. Petrol. 50, 37–59.
Kröner, A., Kovach, V., Belousova, E., Armstrong, R., Dolgopolova, A., Seltmann, R., Alexeiev, D.V., Hoffmann, J.E., Wong, J., Sun, M., Cai, K., Wang, T., Tong, Y., Wilde, S.A., Degtyarev, K.E., Rytsk, E., 2014. Reassessment of continental growth during the accretionary history of the Central Asian Orogenic Belt. Gondwana Res. 25, 103–125.
Larin, A.M., Sal'nikova, E.B., Kotov, A.B., Glebovitsky, V.A., Velikoslavinsky, S.D., Sorokin, A.A., Yakovleva, S.Z., Fedoseenko, A.M., Anisimova, I.V., 2006. Early Cretaceous age of regional metamorphism of the Stanovoi Group in the Dzhugdzhur-Stanovoi Foldbelt: geodynamic implications. Doklady Earth Sciences 409, 727-732.
Leslie, R.A.J., Danyushevsky, L.V., Crawford, A.J., Verbeeten, A.C., 2009. Primitive shoshonites from Fiji: geochemistry and source components. Geochem. Geophys. Geosyst. 10, Q07001. https://doi.org/10.1029/2008GC002326.
Le Voyer, M., Rose-Koga, E.F., Shimizu, N., Grove, T.L., Schiano, P., 2010. Two contrasting H_2O-rich components in primary melt inclusions from Mount Shasta. J. Petrol. 51, 1571–1595.
Likhoidov, G.G., Plyusnina, L.P., Scheka, J.A., Aphanasieva, T.B., 2008. Experimental study of gold and platinum solubility in a complex fluid under hydrothermal conditions. Resour. Geol. 50, 83–92.
Liotard, J.M., Dautria, J.M., Bosch, D., Condomines, M., Mehdizadeh, H., Ritz, J.-F., 2008. Origin of the absarokite-banakite association of the Damavand volcano (Iran): trace elements and Sr, Nd, Pb isotope constraints. Int. J. Earth Sci. (Geologische Rundschau) 97, 89–102.
Liu, J.J., Mao, G.J., Ma, X.H., Guo, Y.Q., Liu, G.Zh., 2008. Discovery of Cu-Ni-Zn-Sn-Fe intermetallic compounds and S-bearing alloys in the Zhaishang gold deposits, southern Gansu Province and its geological significance. Sci. China, Ser. D Earth Sci. 51, 769–777.
Liu, Y., He, D., Gao, C., Foley, S., Gao, S., Hu, Z., Zong, K., Chen, H., 2015. First direct evidence of sedimentary carbonate recycling in subduction-related xenoliths. Sci. Rep. 5 (1547) https://doi.org/10.1038/srep11547.
Lorand, J.-P., Alard, O., Luguet, A., 2010. Platinum-group element micronuggetts and refertilization process in Lherz orogenic peridotite (northeastern Pyrenees, France). Earth Planet. Sci. Lett. 289, 298–310.
Marchesi, C., Garrido, C.J., Harvey, J., Gonzalez-Jimenez, J.M., Hidas, K., Lorand, J.P., Gervilla, F., 2013. Platinum-group elements, S, Se and Cu in highly depleted abyssal peridotites from the Mid-Atlantic Ocean Ridge (ODP Hole 1274A): influence of hydrothermal and magmatic processes. Contrib. Miner. Petrol. 166, 1521–1538.
McCollom, T.M., 2016. Abiotic methane formation during experimental serpentinization of olivine. Proc. Natl. Acad. Sci. 113, 13965–13970.
McInnes, B.I., McBride, J.S., Evans, N.J., Lambert, D.D., Andrew, A.S., 1999. Osmium isotope constraints on ore metal recycling in subduction zones. Science 286, 512–516.
Mogessie, A., Stumpfl, E.F., Weiblen, P.W., 1991. The role of fluids in the formation of platinum-group minerals, Duluth Complex, Minnesota; mineralogic, textural, and chemical evidence. Econ. Geol. 86, 1506–1518.
Nebel, O., Sassi, P.A., Bénard, A., Wille, M., Vroon, P.Z., Arculus, R.J., 2015. Redox-variability and controls in subduction zones from an iron-isotope perspective. Earth Planet. Sci. Lett. 432, 142–151.
Noll, P.D., Newsom, H.E., Leeman, W.P., Ryan, J.G., 1996. The role of hydrothermal fluids in the production of subduction zone magmas: evidence from siderophile and chalcophile trace elements and boron. Geochim. Cosmochim. Acta 60, 587–611.
Nutman, A.P., Chernyshev, A.P., Baadsgaard, H., Smelov, A.P., 1992. The Aldan shield of Siberia, USSR: the age of its Archaean components and evidence for widespread reworking in the mid-Proterozoic. Precambr. Res. 54, 195–210.
Oberthür, T., Melcher, F., Fusswinkel, T., van der Kerkhof, A.M., Sosa, G.M., 2018. The hydrothermal Waterberg platinum deposit, Mookgophong (Naboom spruit), South Africa. Part 1: Geochemistry and ore mineralogy. Mineral. Mag. 82, 725–749.
Page, L., Hattori, K., de Hoog, J.C.M., Okay, A.I., 2016. Halogen (F, Cl, Br, I) behavior in subducting slabs: a study of lawsonite blueschists in eastern Turkey. Earth Planet. Sci. Lett. 442, 133–142.
Parfenov, L.M., VoinovaNatal'in, B.A., Semenov, D.F.,, I.P., 1978. Geodynamics of the North-Eastern Asia in Mesozoic and Cenozoic time and the nature of volcanic belts. Journal of Physics of the Earth 26, S503–S525.
Parkinson, I.J., Hall, G.E.M., Pearce, J.A., 1992. Palladium, platinum, and gold distribution in serpentinite seamounts in the Mariana and Izu-Bonin forearcs: evidence from Leg 125 fluids and serpentinites. In: Fryer, P., Pearce, J.A., Stokking, L.B. et al. Proceedings of the Ocean Drilling Program, Scientific Results 125, 507-518.
Parkinson, I.J., Arculus, R.J., 1999. The redox state of subduction zones: insights from arc-peridotites. Chem. Geol. 160, 409–423.
Pearce, J.A., Peate, D.W., 1995. Tectonic implications of the composition of volcanic arc magmas. Annu. Rev. Earth Planet. Sci. 23, 251–285.
Perchuk, L.L., Aranovich, L.Yu., PodlesskiiLavrant'eva, K.K.I.V., Gerasimov, V.Yu, Fed'kin, V.V., Kitsul, V.I., Karsakov, L.P., Berdnikov, N.V., 1985. Precambrian granulites of the Aldan shield, eastern Siberia, USSR. J. Metamorph. Geol. 3, 265–310.
Peretti, A., Dubessy, J., Mullis, J., Frost, R.B., Trommsdorff, V., 1992. Highly reducing conditions during Alpine metamorphism of the Malenco peridotite (Sondrio, northern Italy) indicated by mineral paragenesis and H_2 in fluid inclusions. Contrib. Miner. Petrol. 112, 329–340.
Piccoli, F., Hermann, J., Pettke, T., Connolly, J., Kempt, E.D., Vieira Duarte, J.F., 2019. Subduction serpentinites release reduced, not oxidized aqueous fluid. Sci. Rep. 9 (1), 19573. https://doi.org/10.1038/s41598-019-55944-8.
Plank, T., Kelley, K.A., Zimmer, M.M., Hauri, E.H., Wallace, P.J., 2013. Why do mafic arc magmas contain ~4 wt.% water on average? Earth Planet. Sci. Lett. 364, 168–179.
Pokrovsky, G.S., Borisova, A.Y., Bychkov, A.Y., 2013. Speciation and transport of metals and metalloids in geological vapors. Rev. Mineral. Geochem. 76, 165–218.
Richards, J.P., 2015. The oxidation state, and sulfur and Cu contents of arc magmas: implications for metallogeny. Lithos 233, 27–45.
Rossetti, P., Zucchetti, S., 1988. Occurrence of native iron, Fe-Co and Ni-Fe alloys in the serpentinite from Balangero asbestos mine (Western Italian Alps). Ofioliti 13, 43–56.
Ryerson, F.J., Watson, E.B., 1987. Rutile saturation in magmas: implications for Ti-Nb-Ta depletion in island-arc basalts. Earth Planet. Sci. Lett. 86, 225–239.
Safonova, I., 2017. Juvenile versus recycled crust in the Central Asian Orogenic Belt: implications from ocean plate stratigraphy, blueschist belts and intra-oceanic arcs. Gondwana Res. 47, 6–27.
Scambelluri, M., Cannaó, E., Gilio, M., 2019. The water and fluid-mobile element cycles during serpentinite subduction: a review. Eur. J. Mineral. 31, 405–428.
Scholten, L., Watenphul, A., Beermann, O., Testemale, D., Ames, D., Schmidt, C., 2018. Nickel and platinum in high-temperature H_2O+HCl fluids: implications for hydrothermal mobilization. Geochim. Cosmochim. Acta 224, 187–199.
Schwarzenbach, E.M., Gazel, E., Goddick, M.J., 2014. Hydrothermal processes in partially serpentinized peridotites from Costa Rica: evidence from native copper and complex sulfide assemblages. Contrib. Miner. Petrol. 168 (1079) https://doi.org/10.1007/s00410-014-1079-2.
Sciortino, M., Mungall, J.E., Muinonen, J., 2015. Generation of high-Ni sulfide and alloy phases during serpentinization of dunite in the Dumont Sill, Quebec. Econ. Geol. 110, 733–761.
Sengör, A.M.C., Natal'in, B.A., Burtman, B., 1993. Evolution of the Altaid tectonic collage and Paleozoic crustal growth in Eurasia. Nature 364, 299–307.
Sharapov, V.N., Kuznetsov, G.V., Timina, T.Yu., Tomilenko, A.A., Chudnenko, K.V., 2017. Simulation of nonisothermal metasomatism of peridotite from mantle wedge beneath the Avacha group of volcanoes (*Kamchatka*). Russ. Geol. Geophys. 58, 551–570.
Sluzhenikin, S.F., Mokhov, A.V., 2014. Gold and silver in PGE-Cu-Ni and PGE ores of the Noril'sk deposits, Russia. Miner. Deposita 50, 465–492.
Snoke, A.W., Quick, J.E., Bowman, H.R., 1981. Bear Mountain igneous complex, Klamath Mountains, California: an ultrabasic to silicic calc-alkaline suite. J. Petrol. 22, 501–552.
Song, Sh., Su, L., Niu, Y., Lai, Y., Zhang, L., 2009. CH_4 inclusions in orogenic harzburgite: evidence for reduced slab fluids and implication for redox melting in mantle wedge. Geochim. Cosmochim. Acta 73, 1737–1754.
Suintilan, N.J., Spangenberg, J.E., Chiaradia, M., Chelle-Michou, C., Stephens, M.B., Fontboté, L., 2019. Petroleum as source and carrier of metals in epigenetic sediment-hosted mineralization. Sci. Rep. 9 (1), 8283. https://doi.org/10.1038/s41598-019-44770-7.

Sun, S.-S., McDonough, W.F., 1989. Chemical and isotopic systematics of oceanic basalts: implications for mantle composition and processes. Geological Soc. London Special Publ. 42, 313–345.

Tagirov, B.R., Filimonova, O.N., Trigub, A.L., Akinfiev, N.N., Nickolsky, M.S., Kvashnina, K.O., Chareev, D.A., Zotov, V.A., 2019. Platinum transport in chloride-bearing fluids and melts: insights from in situ X-ray absorption spectroscopy and thermodynamic modeling. Geochim. Cosmochim. Acta 254, 86–101.

Tang, M., Erdman, M., Eldridge, G., Lee, C.-T.A., 2018. The redox "filter" beneath magmatic orogens and the formation of continental crust. Sci. Adv. 4 https://doi.org/10.1126/sciadv.aar4444.

Tao, R., Zhang, L., Tian, M., Zhu, J., Liu, X., Liu, J., Höfer, H.E., Stagno, V., Fei, Y., 2018. Formation of abiotic hydrocarbons from reduction of carbonate in subduction zones: constraints from petrological observation and experimental simulation. Geochim. Cosmochim. Acta 239, 390–408.

Tao, R., Zhang, L., Zhang, L., 2020. Redox evolution of western Tianshan subduction zone and its effect on deep carbon cycle. Geosci. Front. 11, 915–924.

Tassara, S., González-Jiménez, J.M., Reich, M., Schilling, M.E., Morata, D., Begg, G., Saunders, E., Griffin, W.L., O'Reilly, S.Y., Grégoire, M., Barra, F., Corgne, A., 2017. Plume-subduction interaction forms large auriferous provinces. Nat. Commun. 8 https://doi.org/10.1038/s41467-017-00821-z.

Timm, C., de Ronde, C.E.J., Leybourne, M.I., Layton-Matthews, D., Graham, I.J., 2012. Sources of chalcophile and siderophile elements in Kermadec arc lavas. Econ. Geol. 107, 1527–1538.

Van der Voo, R., van Hinsbergen, D.J.J., Domeier, M., Spakman, W., Torsvik, T.H., 2015. Latest Jurassic – earliest Cretaceous closure of the Mongol-Okhotsk Ocean: a paleomagnetic and seismological-tomographic analysis. Geol. Soc. Am. Spec. Pap. 513, 589–606.

Vernikovsky, V.A., Vernikovskaya, A.E., Pease, V.I., Gee, D.G., 2004. Neoproterozoic orogeny along the margins of Siberia. Geological Society London Memoirs 30, 233–247.

Watkinson, D.H., Melling, D.R., 1992. Hydrothermal origin of platinum-group mineralization in low-temperature copper sulfide-rich assemblages, Salt Chuck intrusion, Alaska. Econ. Geol. 87, 175–184.

Widom, E., Kepezhinskas, P., Defant, M., 2003. The nature of metasomatism in the sub-arc mantle wedge: evidence from Re-Os isotopes in Kamchatka peridotite xenoliths. Chem. Geol. 196, 283–306.

Wilkinson, J.J., Stoffell, B., Wilkinson, C.C., Jeffries, T.E., Appold, M.S., 2019. Anomalously metal-rich fluids from hydrothermal ore deposits. Science 323, 764–767.

Wernette, B., Li, P., Boudreau, A., 2019. Sulfides, native metals, and associated trace minerals of the Skaergaard intrusion, Greenland: evidence for late hydrothermal fluids. Miner. Deposita 55, 1197–1214.

Windley, B.F., Alexeiev, D., Xiao, W., Kröner, A., Badarch, G., 2007. Tectonic models for accretion of the Central Asian Orogenic Belt. J. Geolog. Soc. London 164, 31–47.

Xiao, Y., Sun, Y., Lu, Y., Wen, Ch., Wang, J., 1998. Zinccopperite – a new variety of zinc-copper intermetallic compounds discovered in a porphyry-copper deposit. Acta Geol. Sin. 72, 308–313.

Xie, Y., Hou, Z., Xu, J., Yuan, Zh., Bai, G., Li, X., 2006. Discovery of Cu-Zn, Cu-Sn intermetallic minerals and its significance for genesis of the Mianning-Dechang REE metallogenic belt, Sichuan Province, China. Sci. China, Ser. D Earth Sci. 49, 597–603.

Yang, Y., Meng, F., Xu, X., Robinson, P.T., Dilek, Y., Makeyev, A.B., Wirth, R., Wiedenbeck, M., Cliff, J., 2015. Diamonds, native elements and metal alloys from chromitites of the Ray-Iz ophiolite of the Polar Urals. Gondwana Res. 27, 459–485.

Zhang, Zh., Mao, J., Wang, F., Pirajno, F., 2006. Native gold and native copper enclosed by olivine phenocrysts in a picrate lava of the Emeishan large igneous province, SW China. Am. Mineral. 91, 1178–1183.

Zhang, Ru.Y., Yang, J.-S., Ernst, W.G., JahnIIzuka, Y., Guo, G.-L.,, B.-M., 2016. Discovery of *in situ* super-reducing, ultrahigh-pressure phases in the Luobusa ophiolitic chromitites, Tibet: new insights into deep upper mantle and mantle transition zone. Am. Mineral. 101, 1285–1294.